scientific reports

Check for updates

OPEN

Tuning the physical properties of ternary alloys (NiCuCo) for in vitro magnetic hyperthermia: experimental and theoretical investigation

O. M. Lemine[1]✉, Noura Al-Dosari[1], Saja Algessair[1], Nawal Madkhali[1], Moustapha Elansary[2], Chouaïb Ahmani Ferdi[2], Marzook S Alshammari[3], Rizwan Ali[4], Ali Z. Alanzi[5], Mohammed Belaiche[2] & Kheireddine El-Boubbou[6]

Most of published research on magnetic hyperthermia focused on iron oxides, ferrites, and binary alloy nanostructures, while the ternary alloys attracted much limited interest. Herein, we prepared NiCuCo ternary alloy nanocomposites with variable compositions by mechanical alloying. Physical properties were fully characterized by XRD, Rietveld analysis, XPS, SEM/EDX, TEM, ZFC/FC and H-M loops. DFT calculations were used to confirm the experimental results in terms of structure and magnetism. The results showed that the fabricated nanoalloys are face centered cubic (FCC) with average core sizes of 9–40 nm and behave as superparamagnetic with saturation in the range 4.67–42.63 emu/g. Langevin fitting corroborated the superparamagnetic behavior, while law of approach to saturation (LAS) was used to calculate the magnetic anisotropy constants. Heating effciencies were performed under an alternating magnetic field (AMF, $H_0 = 170$ Oe and $f = 332.5$ kHz), and specific absorption rate (SAR) values were determined. The highest magnetic saturation (M_s), heating potentials, and SAR values were attained for $Ni_{35}Cu_{30}Co_{35}$ containing the lowest Cu but highest Ni and Co percentages, and the least for $Ni_{15}Cu_{70}Co_{15}$. Importantly, the nanoalloys reached the required temperatures for magnetic hyperthermia (42 °C) in relatively short times. We also showed that heat dissipiation can be simply tuned by changing many parameters such as concentration, field amplitude, and frequency. Finally, cytotoxicity viability assays against two different breast cancer cell lines treated with $Ni_{25}Cu_{50}Co_{25}$ nanoalloy in the presence and absence of AMF were investigated. No significant decrease in cancer cell viability was observed in the absence of AMF. When tested against tumorigenic KAIMRC2 breast cancer cells under AMF, the NiCuCo nanoalloy was found to be highly potent to the cells (~ 2-fold enhancement), killing almost all the cells in short times (20 min) and clinically-safe AC magnetic fields. These findings strongly suggest that the as-prepared ternary NiCuCo nanoalloys hold great promise for potential magnetically-triggered cancer hyperthermia.

Keywords Magnetic hyperthermia, Magnetic nanoparticles, Ternary alloys, NiCuCo, SAR, DFT, Ball milling

Magnetic nanoparticles (MNPs) have been widely used for various biomedical applications, particularly for magnetic hyperthermia (MH)[1–4]. MH uses the heat dissipated by MNPs under an alternating magnetic field (AMF) to kill cancerous cells, which compared to the healthy ones are more sensitive to heat in the range of 40–45 °C[5]. The amount of heat produced per unit of time and per unit of gram of magnetic material is known as

[1]Department of Physics, College of Sciences, Imam Mohammad Ibn Saud Islamic University (IMISU), Riyadh 11623, Saudi Arabia. [2]Nanoscience and Nanotechnology Unit, E.N.S Rabat ,Energy Research Centre, Mohammed V University, B.P. 5118, Takaddoum Rabat, Morocco. [3]Micorelectronics and Semiconductors Institute KACST, Riyadh, Saudi Arabia. [4]Medical Research Core Facility and Platforms (MRCFP), King Abdullah International Medical Research Center, King Saud Bin Abdulaziz University for Health Sciences (KSAU-HS), King Abdulaziz Medical City (KAMC), NGHA, Riyadh, Saudi Arabia. [5]Microelectronics and Semiconductors Institute, King Abdulaziz City for Science and Technology (KACST), Riyadh, Saudi Arabia. [6]Department of Chemistry, College of Science, University of Bahrain, Sakhir 32038, Kingdom of Bahrain. ✉email: mamamin@imamu.edu.sa

the specific absorption rate (SAR)[4]. Among the various MNPs, magnetite (Fe_3O_4) and maghemite (γ-Fe_2O_3) are the most studied materials due to their low toxicity, superparamagnetic nature, relatively good SAR values, and ease of synthesis[6–13]. It was found from our group and other reports, that the heating abilities of MNPs under AMF are affected by several parameters such as morphology (e.g., shape, size and size distribution), crystallinity, magnetism (e.g., Curie temperature, saturation magnetization, remanence, coercivity and magnetic anisotropy constant), MNPs concentration, surface modification as well as the amplitudes and frequency of the applied AMF[7–9,13–17]. To keep improving on SAR values, an approach is often used based on the tuning of magnetic saturation, coercivity, and remanence of MNPs by coating with polymers[13] or partial substitution of iron ions by alkaline earth (Gd, Tb, Yb etc.) or transition metals (Ni, Co, Mn, V etc.)[14–19]. Our group looked recently into the effect of doping with Gadolinium (Gd)[14], Cobalt (Co)[15], Aluminium (Al)[16] on SAR of maghemite (γ-Fe_2O_3) NPs. We observed that magnetism and subsequently SAR values of the as-synthesized MNPs can be tuned according to the doped element. For instance, Gd-doped γ -Fe_2O_3 demonstrated a SAR of 120 W/g and quickly attained magnetic hyperthermia temperatures (42 °C), while SAR values of 40 W/g were observed for Al-ZnO-γ-Fe_2O_3 nanocomposites.

Many parameters affect the efficiency of MNPs in hyperthermia applications such as core sizes, Curie temperatures, magnetic saturation, and anisotropy. To enhance heat dissipation, magnetic ternary alloys present an alternative way given the possibility of tuning such parameters. The advantages of these alloys are their potential high saturation and the possibility to tune their Curie temperatures by adding non-magnetic elements. Two main types of magnetic alloys are used: (1) binary alloys AxB1–x which composed of (ferromagnetic-ferromagnetic and/or ferromagnetic-nonmagnetic)[20–24]; (2) ternary magnetic alloys which includes three elements AxByCz. Typically, these types of alloys contain two ferromagnetic elements from the transition metals, while the third element could be non-magnetic or from rare earth elements[25–27]. In fact, only a few reports investigated the heat dissipated by ternary alloys under AMF despite the capability of tuning the Curie temperature, saturation, and coercivity, which directly affects the heating abilities. Salatia et al.[27] reported in their elegant work the tuning of magnetic properties of FexNiyCoz ($17 \le x \le 33$, $21 \le y \le 55$, $12 \le z \le 62$) ternary alloy NPs for hyperthermia. They investigated the magnetic hyperthermia measurements under AMF with intensity of 400 Oe at a frequency of 400 kHz. It was found that SAR values are affected by the composition of Co ranging from 237 to 298 W/g. Kim et al.[26] investigated the heating ability of FexNiyCoz ($17 \le x \le 33$, $21 \le y \le 55$, $12 \le z \le 62$) ternary alloy using an electroless plating method. They optimized the saturation and coercivity through the composition of Ni and found that the best SAR value of 36.5 W/g. Motivated by these and other hyperthermia studies on ternary alloys, we propose to tune the magnetic properties and subsequently the heating of NiCuCo ternary alloys for hyperthermia application.

Herein, we prepare a series of NiCuCo alloy MNPs by mechanical alloying of mixture of Ni, Co, and Cu powders. The structural and magnetic properties of the as-synthesized nanoalloys were fully investigated in details using various spectroscopic and electronic techniques. Rietveld refinement and Density Functional Theory (DFT) calculations were performed to correlate theoretical insights with the observed structural and magnetic properties in these nanoalloys. Heating abilities were investigated as function of NP concentration, frequency, and field amplitude. Furthermore, the cytotoxicity of the prepared nanoalloys on cancerous cells was also investigated. To the best of our knowledge, there is no report on NiCuCo ternary alloys with such complete investigations utilized for hyperthermia application.

Experimental

Samples preparation

A series of $Ni_xCu_{1-2x}Co_x$ (x = 35, 25, 15) alloys were prepared by mechanical alloying technique as shown in Fig. 1. Commercial powders of Co, Cu, and Ni were ball milled in Fritsch machine (P7) with stainless steel. The rotation speed was 350 rpm and the milling process was stopped after every hour for ten minutes in order to prevent overheating. The milling time was 20 h for each sample and the powder to ball ratio was 10:1.

Characterization

XRD analysis was performed using Bruker D8 Discover diffractometer (θ-2θ) equipped with Cu-Kα radiation (λ = 1.5406 Å). Qualitative and quantitative analyses were carried out by the Rietveld method using FULLPROF software programme. The morphology and the composition of the samples were studied by means of TEM (Type JEOL-JEM 1400 operating at 120 kV) and SEM-EDX SEM-SERONAIS1800C model equipped with EDX* systemQuantum Design MPMS-5 S, respectively. SQUID magnetometer (San Diego, CA, USA) was used for the magnetic characterizations. A magnetic field of 100 Oe was applied to record zero-field-cooled and field-cooled (ZFC-FC) curves. The heating efficiency of the samples was performed using a commercial system "Nanotherics Magnetherm" as reported in our previous work[13]. The SAR values are calculated by the following equation[13]:

$$SAR = \frac{\rho\, C_w}{Mass_{MNP}} \left(\frac{\Delta T}{\Delta t} \right) \tag{1}$$

where C_w is the specific heat capacity of water (4.185 J/g.k), ρ is the density of the colloid, $Mass_{MNP}$ is the concentration of the magnetic nanoparticles in the suspension and $\frac{\Delta T}{\Delta t}$ represents the heating rate. By performing a linear fit of temperature increase versus time at the initial time interval (1 to ~30 s), the slope$\Delta T/\Delta t$is obtained.

Synthetic procedure

A series of $Ni_xCu_{1-2x}Co_x$ (x = 35, 25, 15) alloys were prepared by mechanical alloying technique. Commercial powders of Co, Cu, and Ni were ball milled in Fritsch machine (P7) with stainless steel. The rotation speed was

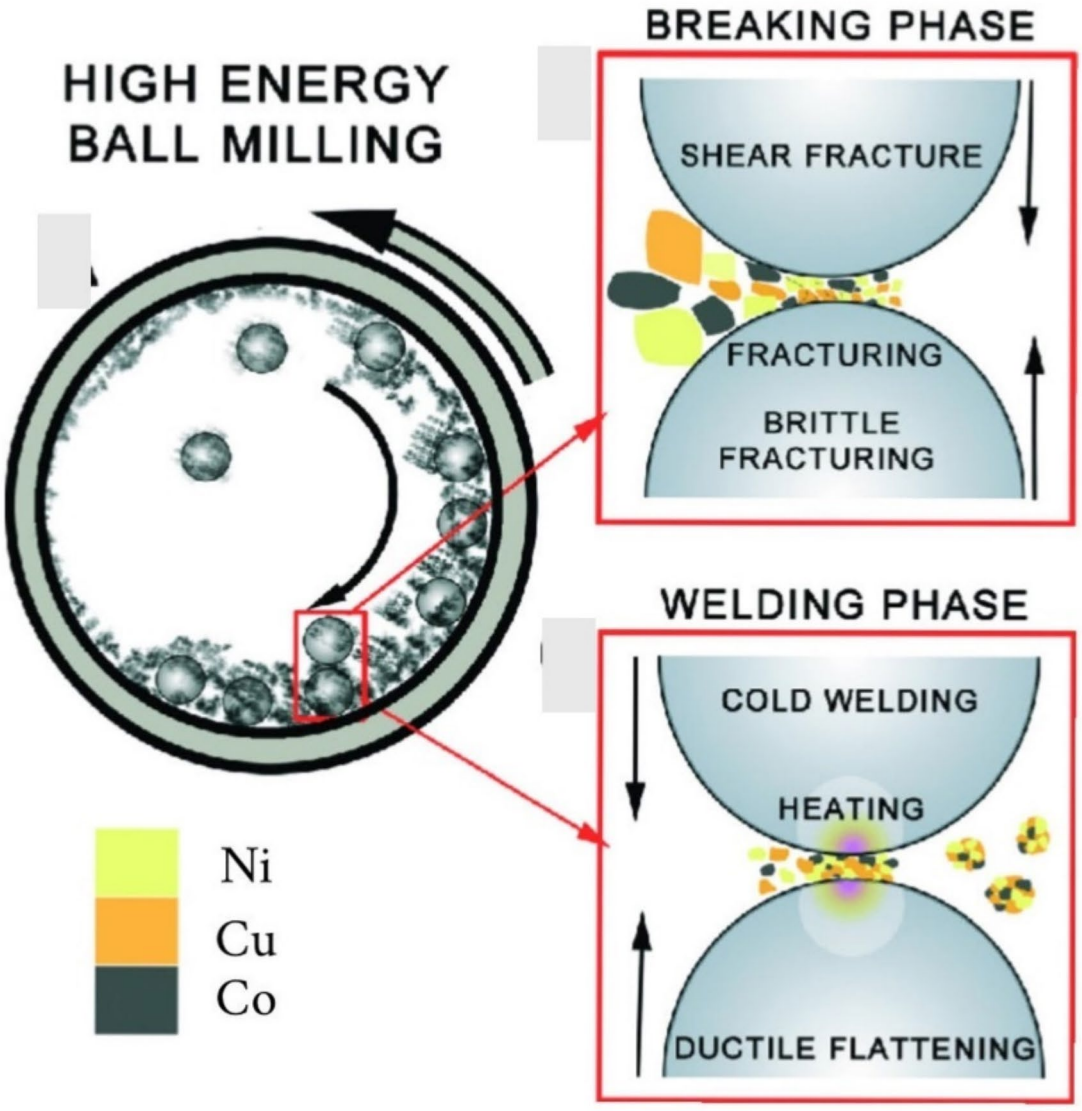

Fig. 1. Schematic diagram for the preparation of nanoalloys using ball milling.

350 rpm and the milling process was stopped after every hour for ten minutes in order to prevent overheating. The milling time was 20 h for each sample and the powder to ball ratio was 10:1.

Cell viability assay

Cell viability of breast cancer MDA-MB-231 and KAIMRC2 cells exposed to nanoalloys was determined using MTT assay. The cell lines were seeded in a 96-well plate at a density of 5×10^5 cells/ well and incubated in a humidified air incubator at 37 °C. Following overnight incubation, cells were treated with graded concentrations of the nanoalloy in 100 µL of supplemented DMEM. Post 48 h incubation, 5 µL of MTT reagent (5 mg/mL) was added to each well and kept for 3 h at 37 °C in the incubator. The media was then removed, and 100ul of dimethyl sulfoxide (DMSO) was added to each well. The absorbance was measured on the Molecular Devices Spectrophotometer absorbance reader at 590 nm for MTT and 650 nm for control. The data was analyzed using GraphPad Prism 8 software and Microsoft excel spreadsheet.

IC_{50} values were calculated from dose-response curves generated using a polynomial dose-response approximation.

Cellular response to hyperthermia

Cellular response to hyperthermia was determined on KAIMRC2 breast cancer cells exposed to $Ni_{25}Cu_{0}Co_{35}$ nanoalloys at 0.25 mg/ml concentration. The cells were trypsinized at a density of 5×10^5 cells/tube, exposed to the compound and subjected to hyperthermia for 15 min. The cells were then seeded in a 96-well plate, incubated in a humidified air incubator at 37 °C and 5% CO_2 and analyzed as before post 48 h of incubation.

Results and discussion

Physical characterization

Structure and morphology

Purity and crystallographic structure formation were confirmed by XRD as shown in Fig. 2a. According to the XRD diffractogram, the indexed diffraction peaks with 2θ values of 43.72°, 50.88° and 75.32° correspond to the (111), (200) and (220) crystal planes, indicating the formation of $Ni_{35}Cu_{30}Co_{35}$, $Ni_{25}Cu_{50}Co_{25}$, and $Ni_{15}Cu_{70}Co_{15}$ alloys with a face-centered cubic (FCC) structure. According to the literature, the synthesis of CoCu, CoNi or NiCuCo alloys can result in a single-phase structure with the coexistence of Co or Ni phases with the other phases (CoCu, CoNi or NiCuCo)[28,29]. In this study, despite the percentage change in Ni, Cu, and Co elements no peaks corresponding to these supplementary phases were observed in the diffractogram of the prepared samples, confirming the formation of a pure phase and the incorporation of the elements Ni, Cu and Co into the FCC structure.

To obtain more information on the crytalographic structure of samples, Rietveld refinement was performed on the XRD diffractogram using the fullprof software (Fig. 2b). It can be seen form the refinement that all samples are crustalyzed in the FCC structure with a space group (F m-3 m). The lattice parameters are almost

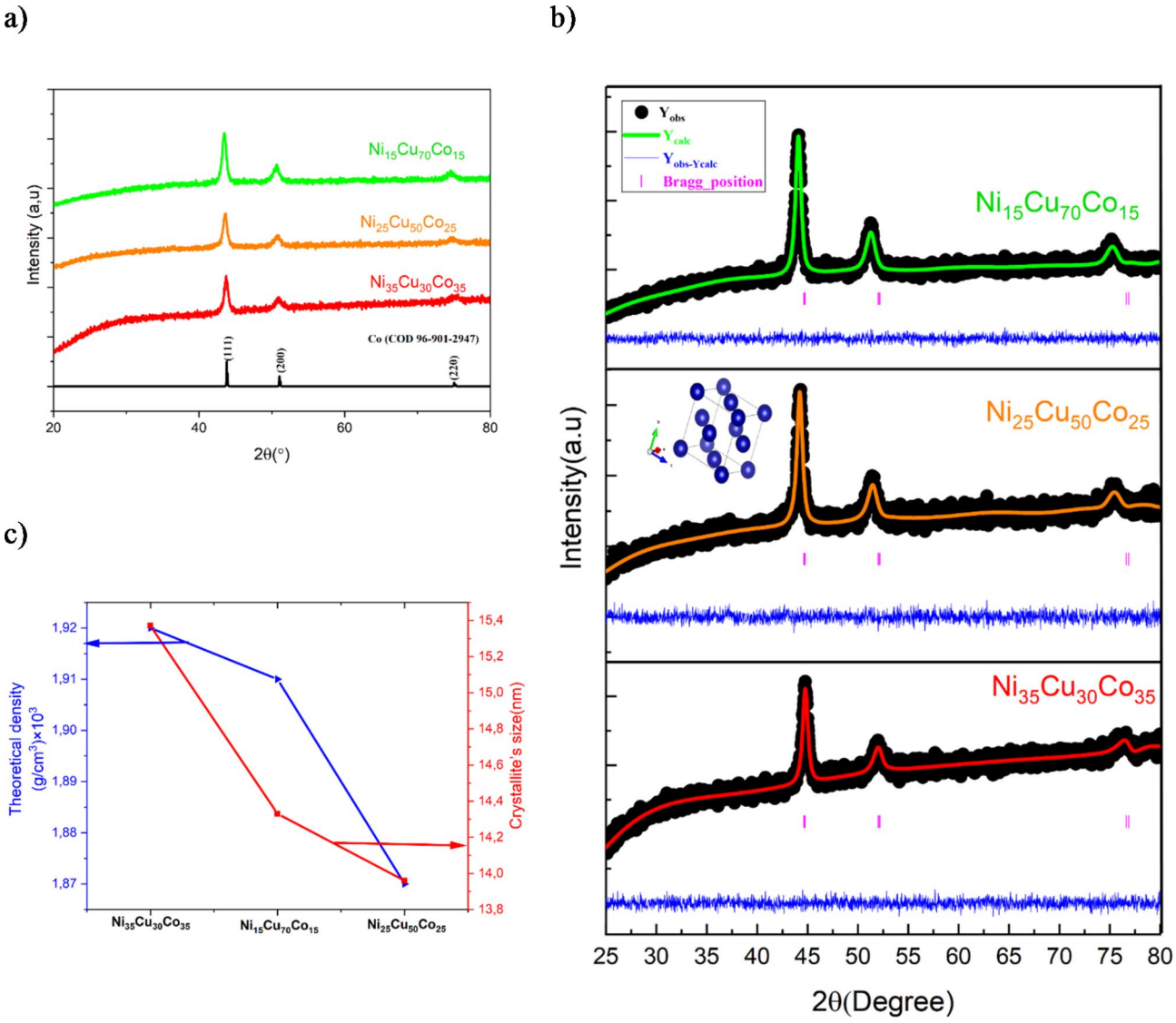

Fig. 2. (**a**) Powder X-ray diffraction patterns of the nanoalloys; (**b**) Rietveld refinement of X-ray diffraction of all samples; and (**c**) crystallite's size variation and theoretical density.

identical and no significant changes were observed, despite the variation in the percentages of the elements Ni, Cu and Co. This can be explained by the fact that the ionic radii of these elements, Ni (0.55 nm), Co (0.58 nm) and Cu (0.57 nm), are practically equal.The crystallite size of the samples is found using the Debye-Scherer (Eq. 2). Theoretical density ρ_{X-ray} is determined by using the Eq. (2)[30]:

$$d = \frac{k\lambda}{\beta .\cos\theta} \tag{2}$$

$$\rho_{X-ray} = \frac{8M}{N\ a^3} \tag{3}$$

where λ is the wavelength of Cu-K_α radiation, β represents the full width at half-maximum, k = 0.9 and θ is the Bragg's angle, M is the molecular weight of the sample, N is the Avogadro's number and a is the lattice parameter.

The structural parameters and crystallite sizes obtained are shown in Table 1. Figure 2c shows a decrease in crystallite sizes as a function of the elements making up the prepared alloys. The decrease in crystallite size in NiCuCo alloys can be attributed to a combination of factors related to enthalpy, binding energy, and other elements. The enthalpy of formation of the elements in the alloy influences their solubility and can lead to the formation of secondary phases that disrupt crystallite growth. The high binding energy of the atoms can make the growth of crystals more difficult by limiting the atomic movements necessary for their expansion. Surface energy, which is affected by surface enthalpy, can also favor smaller crystallite sizes by increasing resistance to growth. In addition, the composition of the alloy, the temperature and cooling rate, as well as mechanical treatments, play a crucial role. The presence of impurities or secondary phases, the thermal and mechanical treatment conditions and the specific properties of the alloy all influence crystallite size[31]. The crystallographic density obtained also showed a decrease (Fig. 2c), due to the change in molecular weight of the samples prepared.

Scanning electron microscopy with energy dispersive X-ray spectroscopy (SEM-EDX) analyses was conducted to verify the elemental composition of the different nanoalloys (Fig. 3). The images reveal different patterns indicating that the surface morphology depends on the concentration of alloys (Fig. 3a–c). EDX spectra elemental confirmed the presence of Ni, Cu and Co elements in the prepared ferrites (Fig. 3d–f). TEM images were then conducted to better identify the morphology and core sizes of the obtained nanoalloys. Delightfully, all the images exhibited a typical quasi-spherical morphology with corresponding narrow size distributions, pinpointing the monodispersity and uniformity of the as-synthesized samples (Fig. 4). Interestingly, while $Ni_{35}Cu_{30}Co_{35}$ showed average NP sizes of ~ 40 nm, $Ni_{25}Cu_{50}Co_{25}$ sizes were found to be ~ 20 nm, and smallest for $Ni_{15}Cu_{70}Co_{15}$ (~ 9 nm). Thus, it seems with decreasing the Cu concentration and increasing Co and Ni cocentrations, the sizes are increasing from 9 to 40 nm.

X-ray photoelectron spectroscopy (XPS)

For an in-depth analysis of the surface composition of the $Ni_xCu_{1-x}Co_x$ alloy, a study using X-ray photoelectron spectroscopy (XPS) was carried out as shown in Fig. 5. The high-resolution Ni 2p spectra reveals two main peaks at 854 and 874.1 eV, corresponding to Ni 2p3/2 and Ni 2p1/2, respectively, with satellite peaks at 861.4 and 879.6 eV indicating the presence of Ni^{2+}. The Cu spectrum shows a main peak at 934 eV, attributed to CuO, and secondary peaks at 943.8, 954.1 and 958 eV, attributed to Cu/Cu_2O, suggesting the minority presence of Cu_2O in the samples. In contrast, the O 1s spectra show a single main peak at 531 eV, with a slight decrease in intensity as the copper concentration increases. This variation in the intensity of the minor peaks is attributed to changes in the oxidation states due to changes in the copper concentration in each sample, confirming the successful formation of the $Ni_xCu_{1-x}Co_x$alloy. The Co 2p spectra show similar characteristics for the three samples studied, with two main peaks at 782 eV and 790 eV, corresponding to Co 2p3/2 and 2p1/2 respectively, this values that are in good agreement with those previously reported in the literature[32–36].

Figure 6 illustrates the deconvolution of the XPS for the sample of $Ni_xCu_{1-x}Co_x$. The peak intensities were estimated based on relevant literature for compounds containing Ni, Co, and Cu. Furthermore, the experimental curve was smoothed, and the background was subtracted before fitting it to the well-known shake-up satellite line of Ni, Co, and Cu. The combination of multi-peaks was obtained through Gaussian fitting. In the Cu 2p3/2 and O 1s regions (Fig. 6b,e,h), the main peak observed at 934 eV for all samples corresponds to CuO, ascribing it to CuO. Additionally, other peaks at 943.8, 954.1, and 958 eV were detected, which could be attributed to Cu/Cu2O. The Cu 2p3/2 binding energy (BE) of 934 eV aligns with the values reported for the Cu-O phase. The larger peak area of the Cu-O fitting peak indicates that Cu-O is the predominant surface composition in this sample. The variations in the intensity of the non-major peaks can be attributed to changes in the oxidation states resulting from alterations in the Cu concentration within each sample. It clearly shows a decrease in the

	a (Å)	cell volume (Å^3)	Theoretical density $\rho_{(X-ray)}$ (g/cm^3) $\times 10^3$	Average crystallite size (nm)
$Ni_{35}Cu_{30}Co_{35}$	3.505	43.09	1.92	15.37
$Ni_{25}Cu_{50}Co_{25}$	3.513	43.39	1.87	13.96
$Ni_{15}Cu_{70}Co_{15}$	3.511	43.28	1.91	14.33

Table 1. Calculated values of the lattice parameter (a), cell volume, and the average crystallite sizes of the nanoalloy samples.

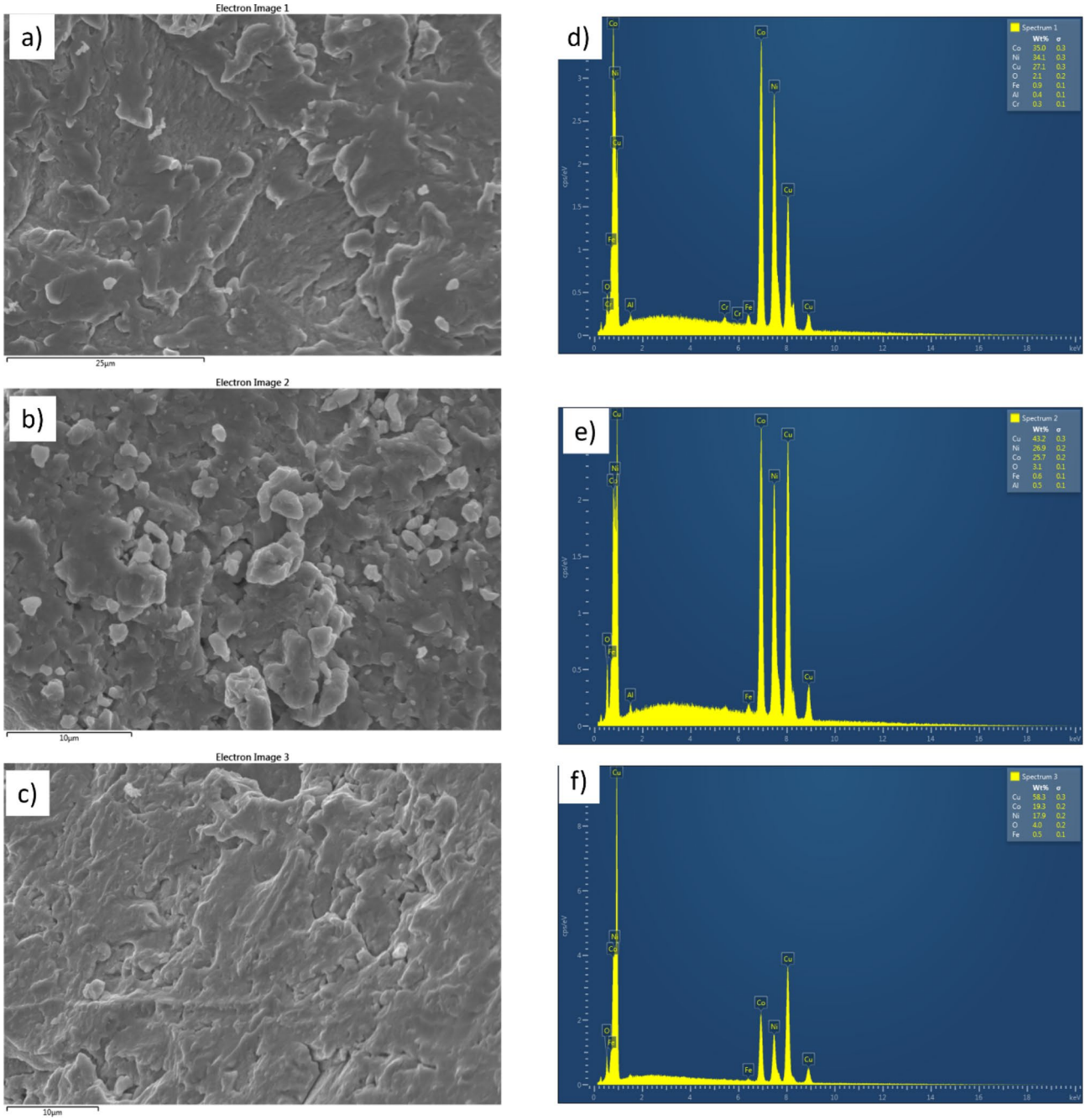

Fig. 3. (**a**–**c**) SEM images and (**d**–**f**) EDX analysis of the different nanoalloys $Ni_{35}Cu_{30}Co_{35}$, $Ni_{25}Cu_{50}Co_{25}$, $Ni_{15}Cu_{70}Co_{15}$.

oxidation process with increasing Cu concentration, which led to the successful formation of NiCuCo alloy. This is consistent with the XRD and FTIR results[34,35]. Various studies[37,38] have shown that the position of these peaks is affected by the chemical composition of the sample, particularly the near environment of the copper cations. Furthermore, the presence of the peak 877 eV bivalent nickel remains in the structure. A second possible explanation for this shift is that the Ni-O bonds weaken when copper concentration is increased to the structure. Indeed, the O 1s region analysis corresponds to Ni and a Ni-Cu Co with the same Ni content (Fig. 6a, d,g).

The XPS spectra of Co2p were obtained, as shown in (Fig. 6c,f,i). The spectra were deconvoluted into four peaks. The first two peaks were centered at 780 eV and 785.5 eV, corresponding to Co 2p3/2 and Co 2p1/2, respectively. The other two peaks were centered at 790 eV and 806 eV, which are characteristic of satellite peaks associated with Co-O materials. These satellite peaks indicate the presence of Co2 + species. However, the peak area corresponding to the number of lower oxygen coordination sites, which can be considered as oxygen defect sites[36], increases with the formation of the alloy. Additionally, the last two peaks at 790 eV and 806 eV expand as the copper concentration increases, as clearly shown in (Fig. 6f,i).

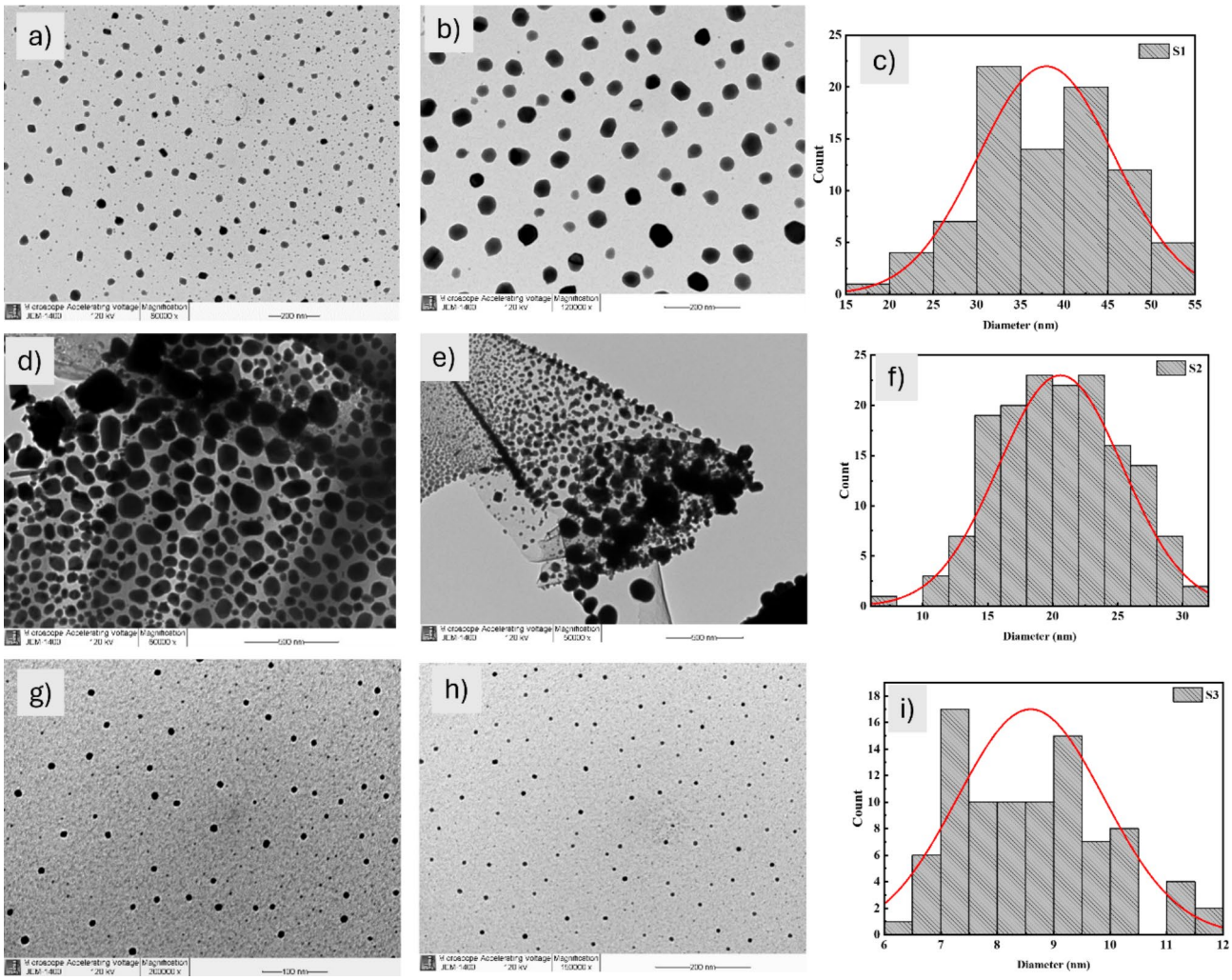

Fig. 4. TEM images at two different magnifications along with corresponding size distributions. (**a**–**c**) $Ni_{35}Cu_{30}Co_{35}$, (**d**–**f**) $Ni_{25}Cu_{50}Co_{25}$, and (**g**–**i**) $Ni_{15}Cu_{70}Co_{15}$.

Magnetic measurements

Magnetic measurements M (T) were performed on the sample using field cooling (FC) and zero field cooling (ZFC) procedures, as shown in Fig. 7. The samples were cooled in a zero magnetic field and then applied to a magnetic field of 100 Oe. The magnetization was measured as the temperature increased (ZFC) and then decreased (FC), over a range of 0–300 K.

The ZFC curves show a gradual increase without saturation being reached in the range measured. The FC increased progressively with decreasing temperature for all the samples, which is associated with the improved magnetic alignment. On the other hand, the ZFC curve first increased then decreased with decreasing temperature for the $Ni_{15}Cu_{70}Co_{15}$ sample and for the other samples it increased with increasing temperature. We also note that the ZFC curves show the peaks that indicate the transition from the blocked state to the unblocked state, with a clearer peak for the $Ni_{15}Cu_{70}Co_{15}$ samples. In addition, the curves overlap at 294, 285, and 104 K, for $Ni_{35}Cu_{30}Co_{35}$, $Ni_{25}Cu_{50}Co_{25}$, and $Ni_{15}Cu_{70}Co_{15}$ respectively, indicating that the T_B blocking temperature decreases as a function of Co and Ni concentrations in the alloys. It can also be deduced that as the Co and Ni concentrations increase, the blocking temperature increases towards room temperature. Decreasing the Co and Ni concentrations in the alloy can effectively lead to a decrease in the magnetic blocking temperature. This is mainly due to the nature of the magnetic interactions in the alloy and how these elements influence these interactions. The blocking temperature is the point at which a magnetic material loses its permanent magnetisation and becomes paramagnetic as the temperature increases. The presence of Co and Ni in an alloy can promote the alignment of the magnetic moments of atoms or ions in the alloy crystal structure, helping to maintain a stable magnetisation. However, if the Co and Ni concentrations are reduced, there are fewer atoms of these elements to participate in these favourable magnetic interactions. This can lead to a disturbance in the alignment of the magnetic moments and a decrease in the blocking temperature. In other words, the alloy would lose its permanent magnetic character at lower temperatures. Similar results have been obtained in the literature by Lee et al. who report that $Ni_{0.72}Co_{0.28}$ and $Ni_{0.14}Co_{0.86}$ alloys show a peak change in magnetic order as the Co content decreases[39]. On the other hand, Arief et al. reported that the blocking temperature of $Ni_{51}Co_{49}$ and is

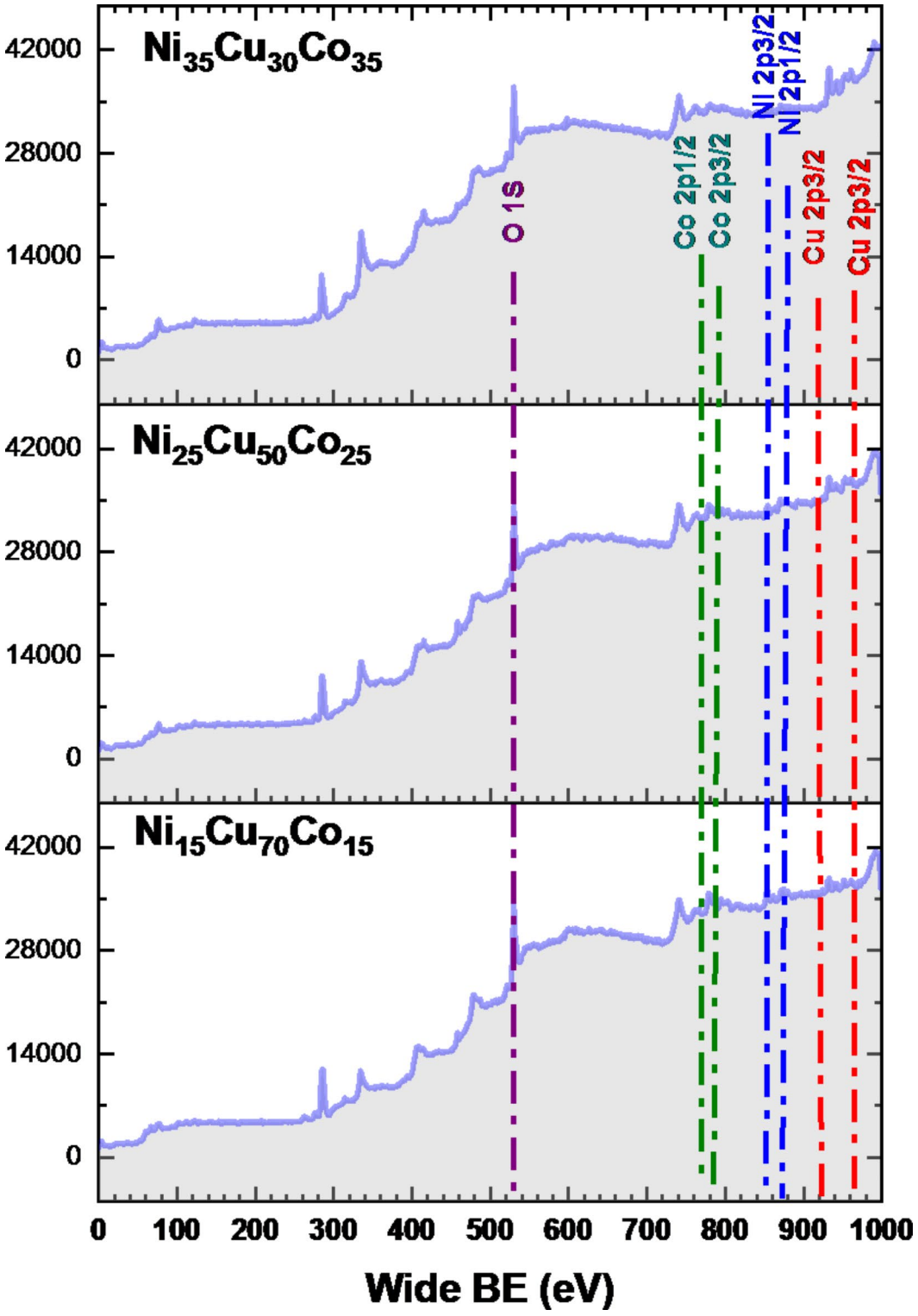

Fig. 5. Wide XPS spectra of the different $Ni_xCu_{1-x}Co_x$ nanoalloys.

of room temperature order[40]. Jayakumar et al. also found that NiCo alloy (50:50) has a blocking temperature of order 290 K[41].

Figure 8a, b shows the M-H curves at room temperature (300 K) and 10 K for the three samples. The main parameters at room temperature are summarized in Table 2. As can be seen at room temperature, the coercivity and remenance are negligible for $Ni_{35}Cu_{30}Co_{35}$ and $Ni_{25}Cu_{50}Co_{25}$ samples indicating superparamagnetic behaviour. In contrast, the sample with a lower Co and Ni concentrations, $Ni_{15}Cu_{70}Co_{15}$, exhibits paramagnetic behaviour[42]. This difference is attributable to a higher concentration of Cu in this sample, which makes it

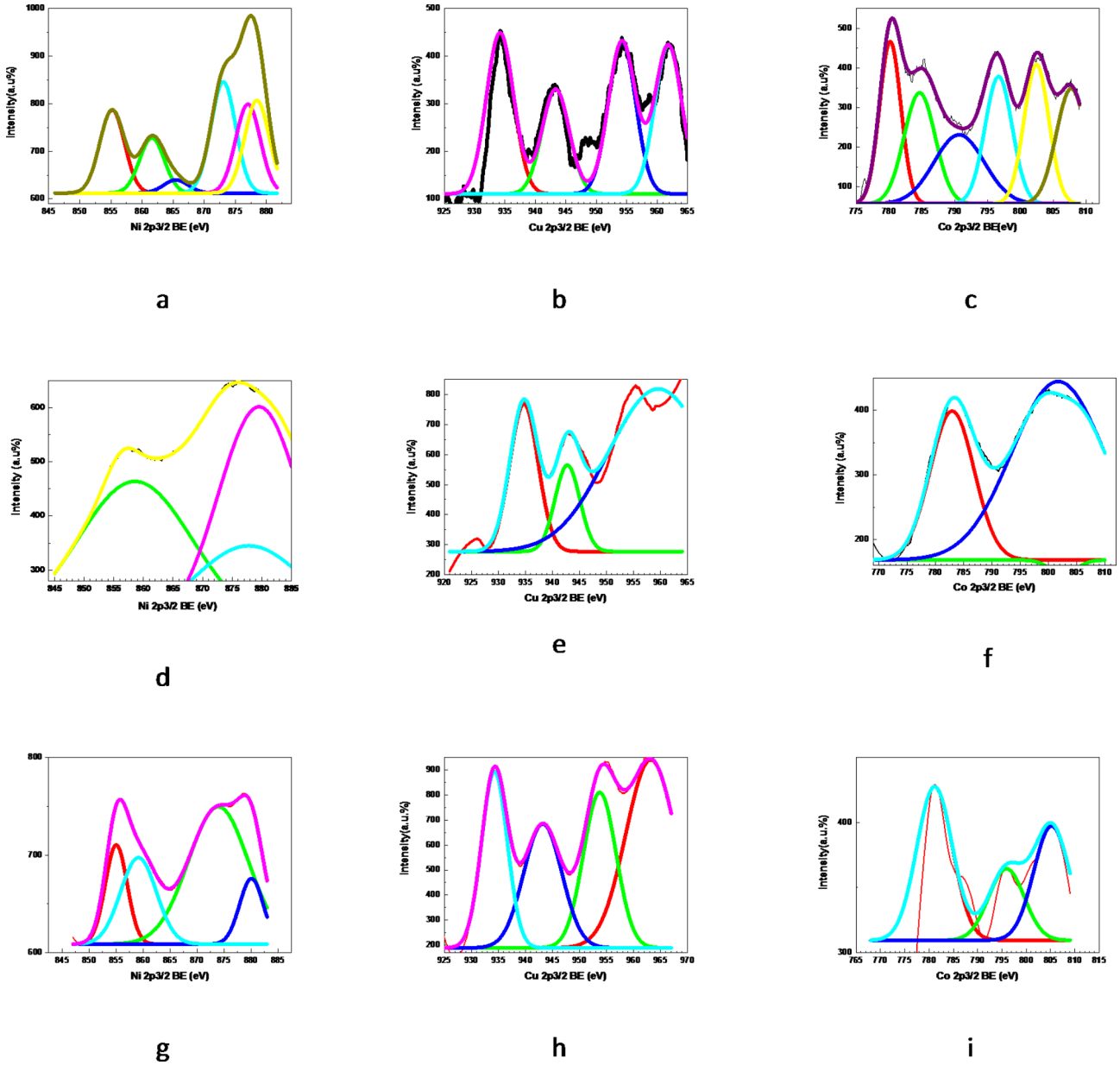

Fig. 6. XPS spectra of high-resolution Ni 2p, Cu 2p and Co 2p.

paramagnetic. On the other hand, at 10 K a transition to ferromagnetic behaviour was observed for all three samples. This result is in perfect agreement with the T_B blocking temperature obtained from the FC-ZFC results. This is therefore a transition temperature between two states, the superparamagnetic state and the blocked (ferromagnetic) state. Magnetic order is therefore not only observed below a temperature T_B, at which the orientation of the magnetic moment of each particle is blocked[42].

The shift in blocking temperature towards room temperature for the $Ni_{25}Cu_{50}Co_{25}$ and $Ni_{35}Cu_{30}Co_{35}$ samples can be attributed to several subtle but significant factors. Although the average crystallite sizes are close (14.33 nm for $Ni_{15}Cu_{70}Co_{15}$, 13.96 nm for $Ni_{25}Cu_{50}Co_{25}$, and 15.37 nm for $Ni_{35}Cu_{30}Co_{35}$), the slight variation in crystallite size could influence the magnetic anisotropy, contributing to a higher blocking temperature. In addition, the theoretical density (1.91 g/cm³ for $Ni_{15}Cu_{70}Co_{15}$) and crystal lattice volume (43.28 Å³) indicate that small differences in crystal structure and element distribution can affect dipolar interactions between nanoparticles, enhancing magnetic stability and shifting the blocking temperature closer to room temperature. The cobalt (Co) and nickel (Ni) content also plays a key role, with 15% Ni and 15% Co for $Ni_{15}Cu_{70}Co_{15}$, compared with 25% Ni and Co for $Ni_{25}Cu_{50}Co_{25}$, and 35% for $Ni_{35}Cu_{30}Co_{35}$. Higher Ni and Co contents generally increase magnetic anisotropy, which can stabilize the alignment of magnetic moments at higher temperatures. These combined effects, although subtle, are sufficient to explain the distinct magnetic behavior of $Ni_{15}Cu_{70}Co_{15}$ compared with other compositions.

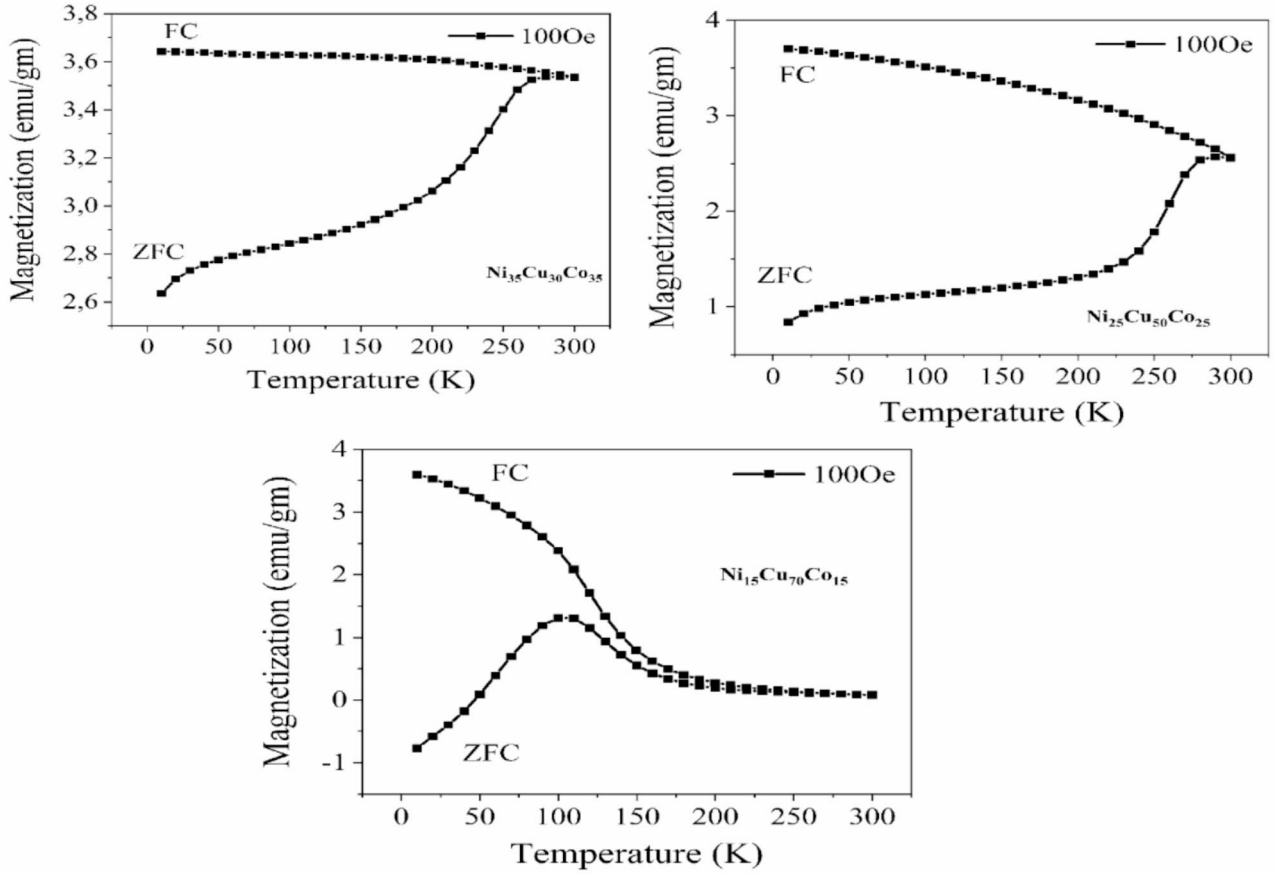

Fig. 7. ZFC/FC curves at 100 Oe.

The saturation magnetization (M_S) was determined using the saturation approach law[43]. The values obtained for the measurement at 300 K are as follows: 42.63 emu/g for the $Ni_{35}Cu_{30}Co_{35}$ sample, 21.49 emu/g for the $Ni_{25}Cu_{50}Co_{25}$ sample, and 4.73 emu/g for the $Ni_{15}Cu_{70}Co_{15}$ sample. It is clear that saturation magnetization depends on Co and Ni concentrations due to the magnetic nature of these elements, with Co^{2+} ($3\mu_B$) and Ni^{2+} ($2\ \mu_B$) having a magnetic moment while Cu^{2+} is non-magnetic. On the other hand, at a temperature of 10 K an increase in saturation magnetisation was observed and the values found were 45.97, 33.04, 19.06 emu/g for the $Ni_{35}Cu_{30}Co_{35}$, $Ni_{25}Cu_{50}Co_{25}$, and $Ni_{15}Cu_{70}Co_{15}$ samples respectively. This increase is due to the alignment of the magnetic moments parallel to the direction of the applied magnetic field, which is caused by the decrease in thermal energy as the temperature decreases[44].

To confirm the superparamagnetic behavior, the experimental magnetization values are fitted with Langevin's theory of paramagnetism by using the following function:

$$M = M_s \coth\left(\frac{m_{np}H}{K_BT}\right) - \frac{K_BT}{m_{np}H} \tag{4}$$

where, $M_s$is the magnetic saturation, m_{np} is the nanoparticle magnetic moment, T is the temperature and K_B is the Boltzman constant. The M(H) curve successfully fits into the Langevin model, as demonstrated by an example of the fitting of the experimental magnetization of $Ni_{25}Cu_{50}Co_{25}$ (Fig. 8c).

Finally, we determined the magnetic effective anisotropy constant (K_{eff}) by using law of approach to saturation (LAS), which describes the magnetization near the saturation and can be written as follows:

$$M(H) = M_s\left(1 - \frac{b}{H^2}\right) \tag{5}$$

where the parameter b can be used to determine K_{eff} using the following formula:

$$K_{eff} = \mu_0 M_s\sqrt{\frac{15b}{4}} \tag{6}$$

An example of fitting is displayed in Fig. 8d and the obtained values of K_{eff} are displayed in Table 2.

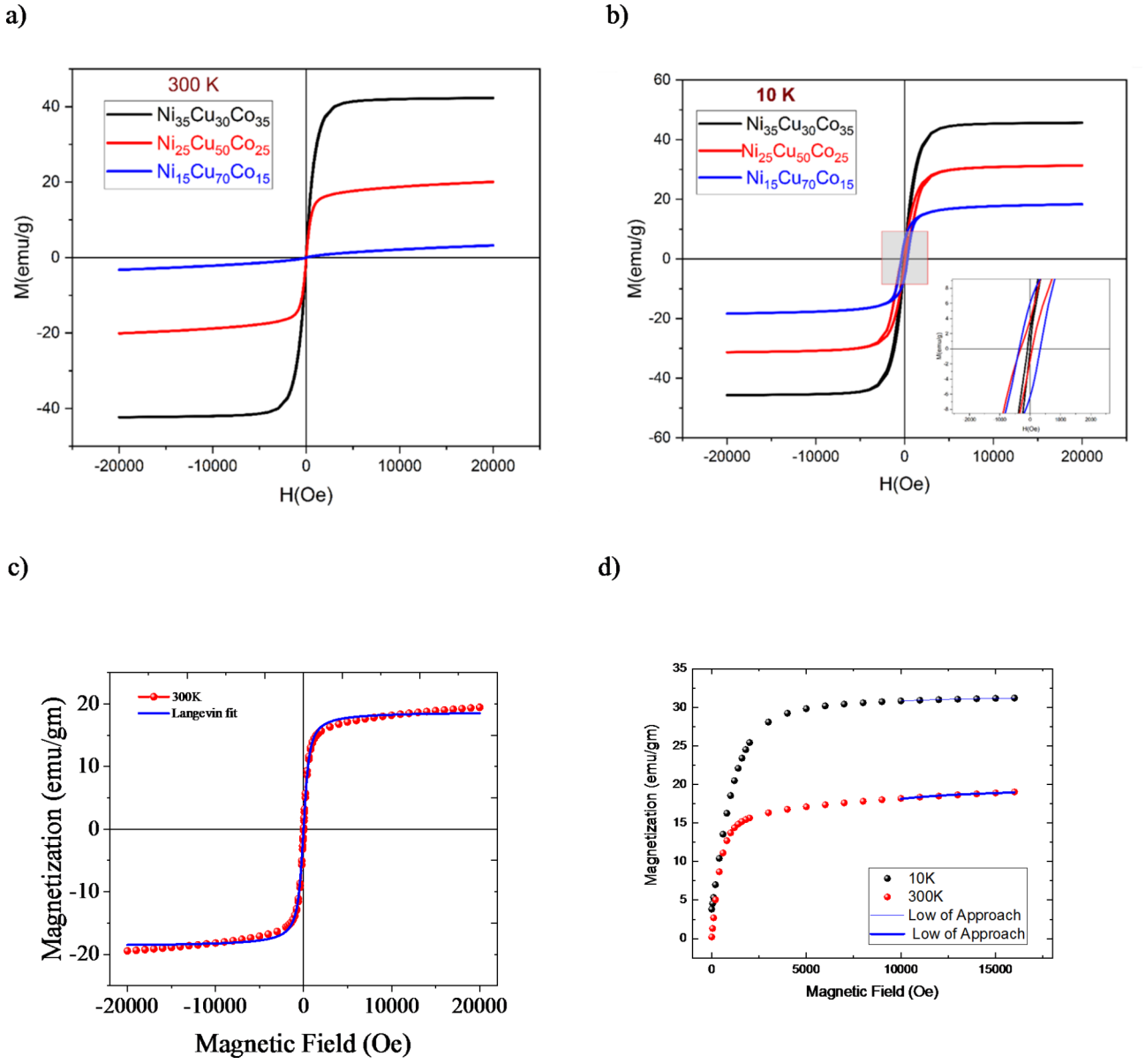

Fig. 8. Magnetization hysteresis loops of the different NiCuCo nanoalloys at (**a**) T = 300 and b) 10 K. (**c**,**d**) an example of (**c**) Langevin fitting and (**d**) Law of approach to saturation (LAS) for $Ni_{25}Cu_{50}Co_{25}$.

Samples	Experimental			Langevin method	Law of approach to saturation (LAS)	
	H_c(Oe)	M_r(emu/g)	M_s(emu/g)	M_s(emu/g)	M_s(emu/g)	K_{eff}(erg/cm^3)
$Ni_{35}Cu_{30}Co_{35}$	5.791	0.458	42.55	42.66	42.43	8.964×10^4
$Ni_{25}Cu_{50}Co_{25}$	7.433	0.223	19.53	18.74	19.48	9.9462×10^4
$Ni_{15}Cu_{70}Co_{15}$	1.669	1.081	3.31	Not fitting due to paramagnetic behaviour	3.92	6.4611×10^4

Table 2. Magnetic parameters deduced from experimental, Langevin function fitting, and law of approach to saturation fitting for $Ni_{1-x}Cu_xCo_{1-x}$ samples at room temperature.

Density functional theory (DFT) study

We performed DFT calculations using the Wien2k package[45] to correlate the structural, magnetic, and electronic properties of the prepared alloys with experimental results. The ion-electron interaction was described with the Full-Potential Linear Augmented Plane Wave (FP-LAPW) method. For the structural optimization of the studied systems, the exchange-correlation potential was approximated by the Perdew–Burke–Ernzerh of[46] and

Wu-Cohen[47] in the Generalized Gradient Approximations (PBE-GGA) and (WC-GGA) respectively. For the magnetic and electronic properties, the PBE-GGA method was employed. The Muffin-tin radii (RMT) were chosen to be 2.34 atomic units (a.u.) for Nickel (Ni), Copper (Cu) and Cobalt (Co). The energy cut-off parameter of the matrix size was set at $R_{MT} \times K_{max} = 8$. The Brillouin zone (BZ) was sampled on a tetrahedral mesh with at least 16,000 k-points/number of atoms in unit cell. The energy threshold between the core and the valence states was set at −6 eV. The convergence criteria were chosen to be $10^{-3}e$ (e: electron-charge) for charge density and 10^{-6} Ry (Ry: Rydberg) for energy. The plots of the density of states were created with the software Grace[48], whereas the schematic diagrams of the structures under study were constructed using VESTA software[49].

The studied systems crystallize in FCC structure with the space group Fm-3 m. To evaluate the structural, magnetic, and electronic properties of the systems: $Ni_{35}Cu_{30}Co_{35}$, and $Ni_{15}Cu_{70}Co_{15}$, we constructed (2×1×1) supercells containing 8 atoms per cell. The corresponding equivalent formulae were $Ni_{37.5}Cu_{25}Co_{37.5}$ and $Ni_{12.5}Cu_{75}Co_{12.5}$ respectively, which shall be referred to further in the text by Cu30 and Cu70, respectively. For $Ni_{25}Cu_{50}Co_{25}$, we used a unit cell of 4 atoms with matching equivalent formula, which shall be referred to by Cu50. The schematic diagrams of the studied systems are displayed in Fig. 9.

Different configurations with different atomic arrangement need to be considered due to the change in Cu concentration in NiCuCo alloy. For Cu25, it is observed that Ni, Cu, and Co atoms are dispersed randomly with high energy for configuration, and hence less stability. To lower the energy of their structure, the calculations show that Ni, Cu and Co atoms tend to arrange themselves in layers to some extent. For Cu50, the structure tends to form alternating Cu layers and Ni-Co layers. Lastly, for Cu75, the configurations where Ni and Co are nearest neighbors have lower total energy than those where Ni and Co are next-nearest neighbors. In conclusion, we find that Ni, Co and Cu atoms tend to arrange themselves in alternating Cu and Ni/Co layers. For increasing Cu concentration, Ni and Co tend to form aggregates rather than to be dispersed. We performed lattice optimization by using the WC-GGA and the PBE-GGA methods and the results are analyzed and compared with the experimental values. It is important to highlight that previous works reported that that the WC-GGA method gives more precision in determining structural properties compared to LDA or even PBE-GGA[50], while PBE-GGA method tend to overestimate the lattice volume[51].

Figure 10 depicted the lattice optimization of the studied systems using both methods. It can be seen and as expected, the PBE-GGA method tends to overestimate the lattice volume compared to the WC-GGA method. Table 3 summarized the calculated lattice parameter "a" as well as its corresponding error with respect to the experimental data from the alloys. It can be observed that the results from WC-GGA and PBE-GGA calculations indicate that the lattice volume increases when Cu concentration increases, the same trend is observed experimentally. However, the values obtained from WC-GGA agree with those deduced from the experiments compared to that calculated by PBE-GGA method. Moreover, these results are in very good agreement with experiment, with deviations as low as 0.2%. This proves that WC-GGA is more accurate than PBE-GGA for structural optimization of Ni-Cu-Co ternary alloy systems, and probably for other transition metal alloys.

Furthermore, we determined the magnetic properties of the studied alloy systems by using PBE-GGA method. Table 4 displays the total magnetic moment M_{tot} per 4 formula units of the systems under study in units of μ_B and emu/g, we converted from Bohr magneton to emu/g to be able to compare it with the experimental saturation magnetization M_S in emu/g. The table also lists the spin magnetic moments of Ni, Co and Cu in μ_B. These values were obtained using the PBE-GGA method in the ferromagnetic spin ordering. We observe that the total magnetic moment of Cu70 is very close to experiment, and as the Cu concentration decreases (Cu50 and Cu30), M_{tot} increases, which is expected given that diamagnetic Cu is being replaced with magnetic Ni and Co. The same increase in M_S is observed experimentally, however, as the Cu content increases, the deviation of M_{tot} from the experimental M_S increases significantly. This might be explained by the existence of magnetic exchange interactions, which are not considered in the calculations, that goes against the total alignment of the magnetic spins of Ni and Co. The consideration of the orbital moment of Co and Ni can be discarded due to their weak contribution[52,53]. The spin magnetic moments of Ni and Co slightly increases going from Cu70 to Cu50 and to Cu30. The obtained values are close to those found for Co and Ni in $FeCoNi(MnAl)_x$ alloy systems[54].

Finally, we investigated the electronic structure of the nanoalloys by calculating the total density of states (DOS) and partial density of states (PDOS) of Ni, Co, and Cu LAPW spheres in the studied Ni-Cu-Co ternary alloy systems. Figure 11 shows the DOS and PDOS of Ni, Co and Cu LAPW spheres in the studied Ni-Cu-Co ternary alloy systems. As expected, the electronic structure of all the studied systems reveals a metallic behavior, in addition, the spin up and spin down states are not symmetrical, reflecting the magnetic nature of

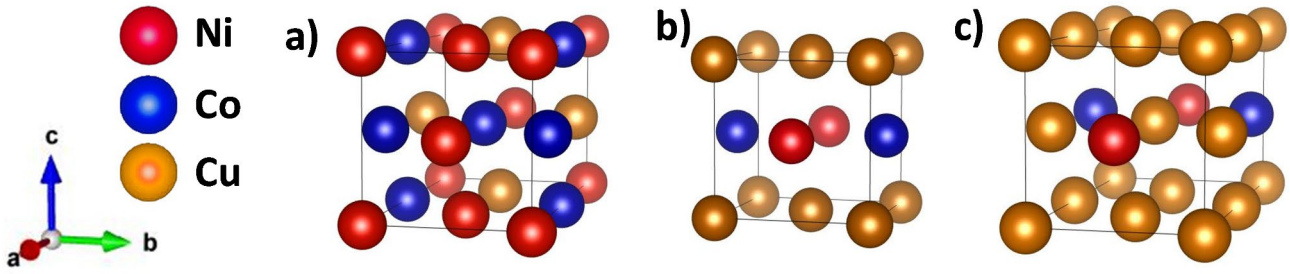

Fig. 9. Schematic diagrams of the NiCuCo ternary alloy structures (**a**) Cu30; (**b**) Cu50; and (**c**) Cu70.

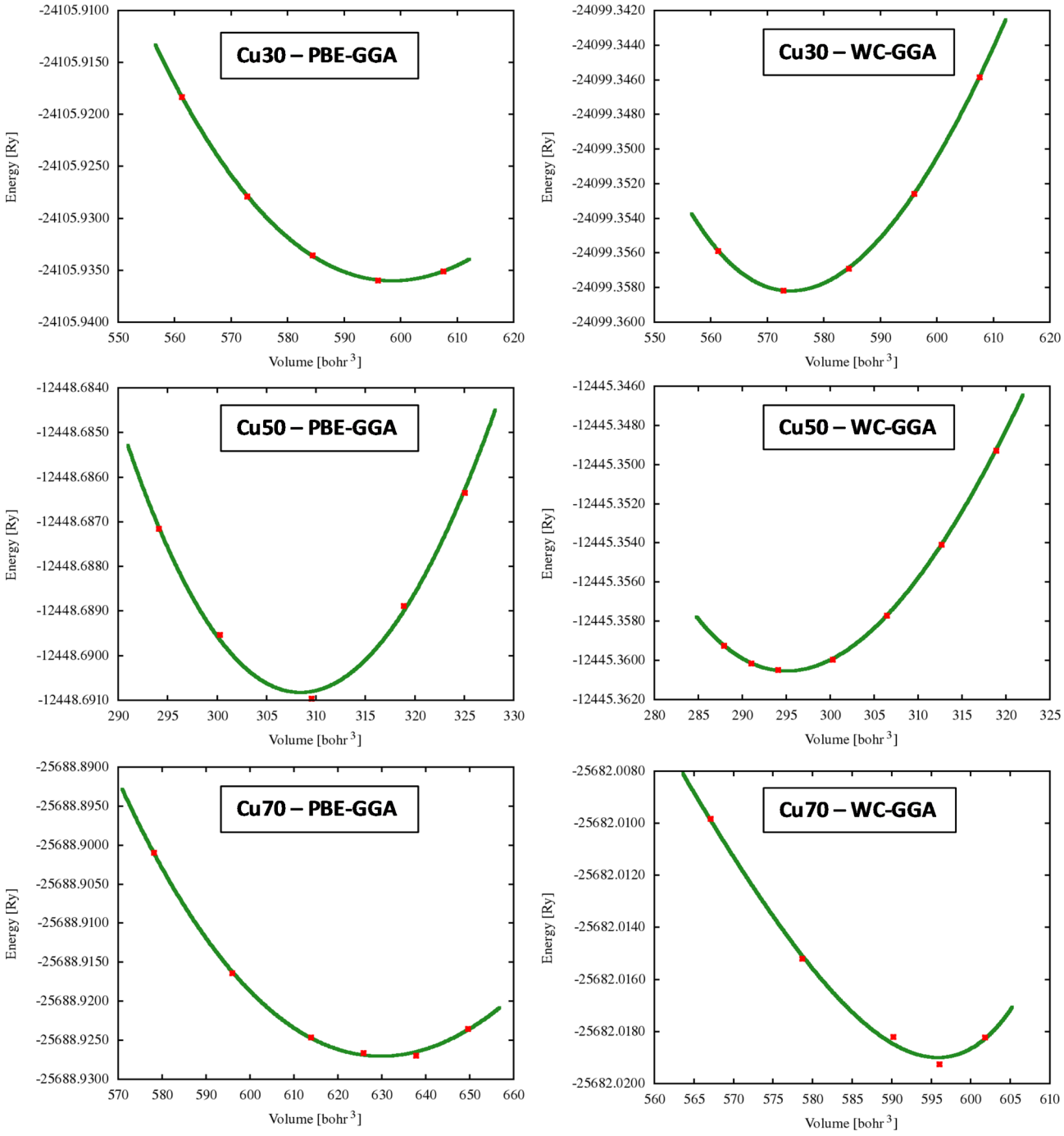

Fig. 10. Total energy as a function of volume of the studied systems using the PBE-GGA and WC-GGA methods.

the nanoalloys. For all systems, the PDOS of Cu is quite symmetrical, reflecting the diamagnetic nature of Cu in the systems ($M(Cu) = 0.03\ \mu_B$), the exception here is with Cu50 where the PDOS of Cu is less symmetrical, especially is energy range from -2 eV to 1 eV. This is reflected in a slightly higher spin magnetic moment ($M(Cu) = 0.08\ \mu_B$).

For the PDOS of Ni, we find that Ni states are asymmetrical, especially around the Fermi level for Cu50 and Cu70, which is associated with the magnetic nature of Ni in these systems ($M(Ni) \approx 0.5\ \mu_B$ and $0.3\ \mu_B$ respectively). In addition, Ni spin up states do not change significantly when the Cu concentration increases. These states extend from -6 eV to the Fermi level with a peak centered around 1 eV below the Fermi level. However, Ni spin down states undergo changes when the Cu concentration increases. Indeed, in Cu30, Ni states are delocalized and extend to 1 eV above the Fermi level, however, as the Cu content increases, we observe a splitting of Ni states giving rise to two peaks below and at the Fermi level, indicating more localized states. We

	System	a (Å)	a_{exp} (Å)	Error (%)	B (GPa)	V (Å^3)	V_{exp} (Å^3)
PBE-GGA	Cu30	3.53466	3.505	0.85	204.088	44.16	43.09
	Cu50	3.57983	3.511	1.96	156.3555	45.88	43.28
	Cu70	3.61528	3.513	2.91	165.0271	47.25	43.39
WC-GGA	Cu30	3.48829	3.505	0.48	222.3901	42.45	43.09
	Cu50	3.51915	3.511	0.23	202.579	43.58	43.28
	Cu70	3.53466	3.513	0.62	317.6368	44.16	43.39

Table 3. Calculated lattice parameter "a" in Å, error with respect to experiment in %, bulk modulus B in GPa, lattice volume V in Å^3. Experimental data from the present work is also included.

	M_{tot} (μ_B)	M_{tot} (emu/g)	M_S (emu/g)*	M(Ni) (μ_B)	M(Co) (μ_B)	M(Cu) (μ_B)
Cu30	3.231	75.20	45.97	0.531	1.672	0.036
Cu50	2.162	49.34	33.04	0.539	1.572	0.058
Cu70	1.835	20.54	19.06	0.331	1.484	0.014

Table 4. Calculated total magnetic moment M_{tot} per 4 formula units in Bohr magneton (μ_B) and in emu/g, compared to the experimental saturation magnetization M_S in emu/g, as well as spin magnetic moments of Ni, Co and Cu in μ_B, calculated using the PBE-GGA method. *Experimental values from the present work.

also observed that Co states are asymmetrical to a larger extent, which is associated with a higher spin magnetic moment for Co (M(Co) ≈ 1.5 μ_B). In addition, the peak in the spin down channel shifts to lower energy levels as the concentration of Cu increases in the alloy system.

.

Hyperthermia measurements

The heating efficiencies of the nanoalloy samples dispersed in water under AMF were evaluated as function of concentration, frequency, and field amplitude. Figure 12 shows the temperature rise of $Ni_{35}Cu_{30}Co_{35}$, $Ni_{25}Cu_{50}Co_{25}$, $Ni_{15}Cu_{70}Co_{15}$ nanoalloys during 15 min under frequency of 332.5 kHz, magnetic field of 170 Oe, and concentration of 10 mg/mL. The parameters deduced from the temperature rise are summarized in Table 5. The following remarks can be highlighted:

(i) The heating curves of all samples show two parts (Fig. 12a), a sharp temperature increase occurring during the first 30 s followed by a gradual increase of temperature. The first component of the heating curve is due to the alignment of particles under AMF, while the second part is related to the different mechanisms which lead to heat dissipation. Similar behavior was observed for binary and ternary alloys[26,27].
(ii) All samples except $Ni_{15}Cu_{70}Co_{15}$ reach the temperature required for magnetic hyperthermia application (42 °C), after short time of the application of AMF. It is important to note that reaching this temperature in a short time is very crucial for the hyperthermia applications due to the short time of the exposition of magnetic field. It is important also to highlight that $Ni_{15}Cu_{70}Co_{15}$ can reach easily hyperthermia temperatures when a longer time of AMF is applied.
(iii) All the samples present relatively good values of SAR, where the highest value was obtained for $Ni_{35}Cu_{30}Co_{35}$ and lowest for sample with highest concentration of Cu (Fig. 12b). Generally, SAR depends on many parameters such as magnetization, size, shape, magnetic anisotropy constant etc. As shown in Fig. 12c, there is a perfect correlation between SAR and magnetization (M_s) for all the samples. The highest SAR is obtained for nanoalloys with the highest magnetic saturation, as has been observed earlier by us and others.

To avoid overheating during hyperthermia measurements, we selected the nanoalloy $Ni_{25}Cu_{50}Co_{25}$ with middle heating characteristics for further investigation and later for in vitro hyperthermia. Figure 13a displays the temperature rise under different field amplitudes at constant frequency $f = 332$ kHz. As can be observed, the magnetic hyperthermia frame is reached only at high field (140 and 170 Oe). As expected, SAR values increased with increasing field amplitude (Fig. 13b), indicating the possibility to tune the heating efficiencies by changing field amplitude. Furthermore, Fig. 13c, d shows the temperature rise and SAR values at different frequencies (113, 170 and 332 kHz) but at constant field amplitude of $H_o = 130$ Oe. As indicted, the same trend of temperature rise and SAR for increasing field amplitude is observed again for different frequencies. At a frequency of 332 kHz, the nanoalloy exhibits the highest SAR value and reach magnetic hyperthermia in relatively short times (12 min) while at lower frequencies (113 kHz and 332 kHz), the nanoalloys did not reach the hyperthermia temperature of 42 °C within the period of 30 min.

We also tested heating abilities at two different concentrations (2.5 and 5 mg/mL). Figure 14a displays the temperature rise of the two different concentrations under AMF with $f = 332.8$ kHz and $H_0 = 170$ Oe. As can be seen, even at the lowest concentration tested, a good heating abilities were observed, where magnetic

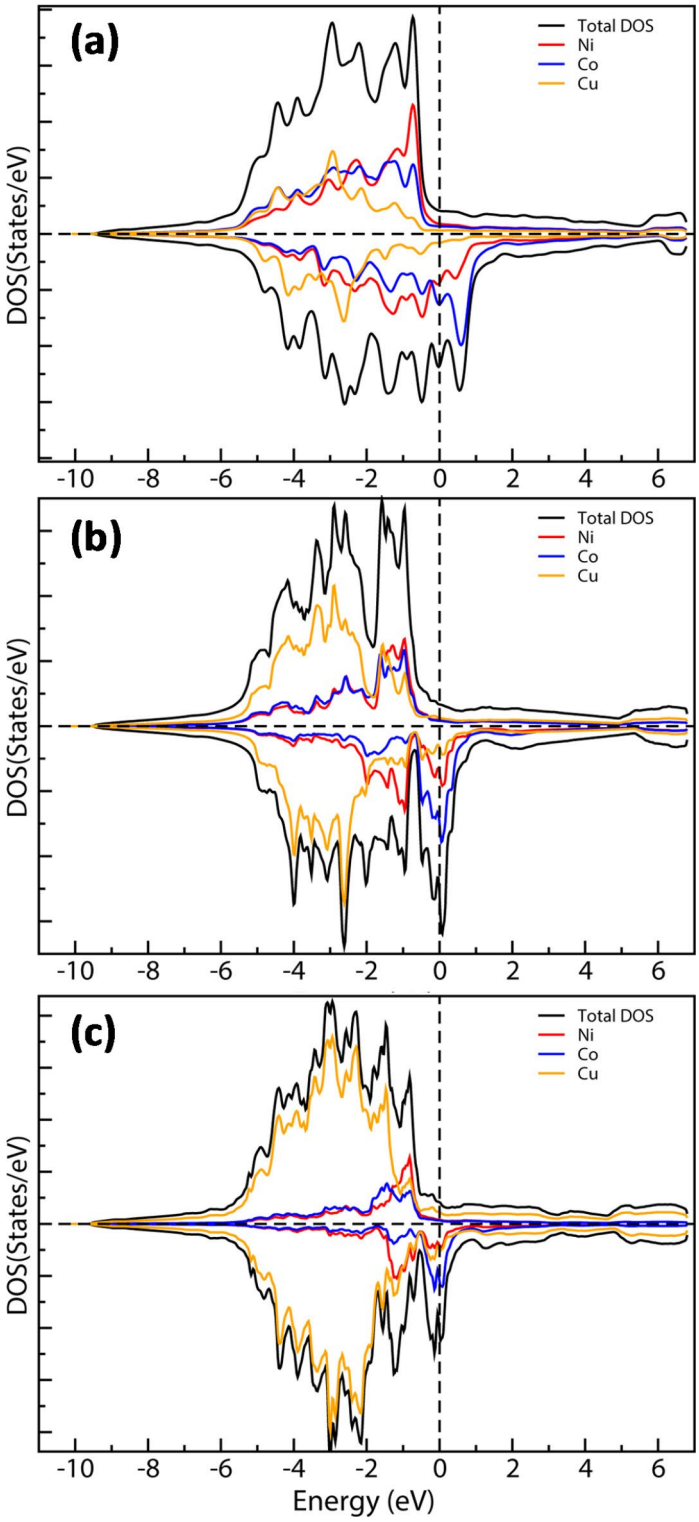

Fig. 11. DOS and PDOS of Ni, Co, and Cu LAPW spheres in NiCuCo ternary alloy systems: (**a**) Cu30; (**b**) Cu50; (**c**) Cu70.

hyperthermia temperatures were reached in relatively short times. The maximum temperature increased from 46.32 to 52 °C when the concentration increased from 2.5 to 5 mg/mL, respectively. The increase in temperature with increasing concentration can be explained by the additional amount of MNPs, which is generally the main source of heat under AMF as the MNPs return to their relaxed states. Interestingly, SAR values increased with decreasing the concentrations, as they were found to be equal to 356 and 256 W.g-1 for 2.5 and 5 mg/ml, respectively (Fig. 14b). As reported by early reports[10,13], the increase of SAR with decreasing concentration of

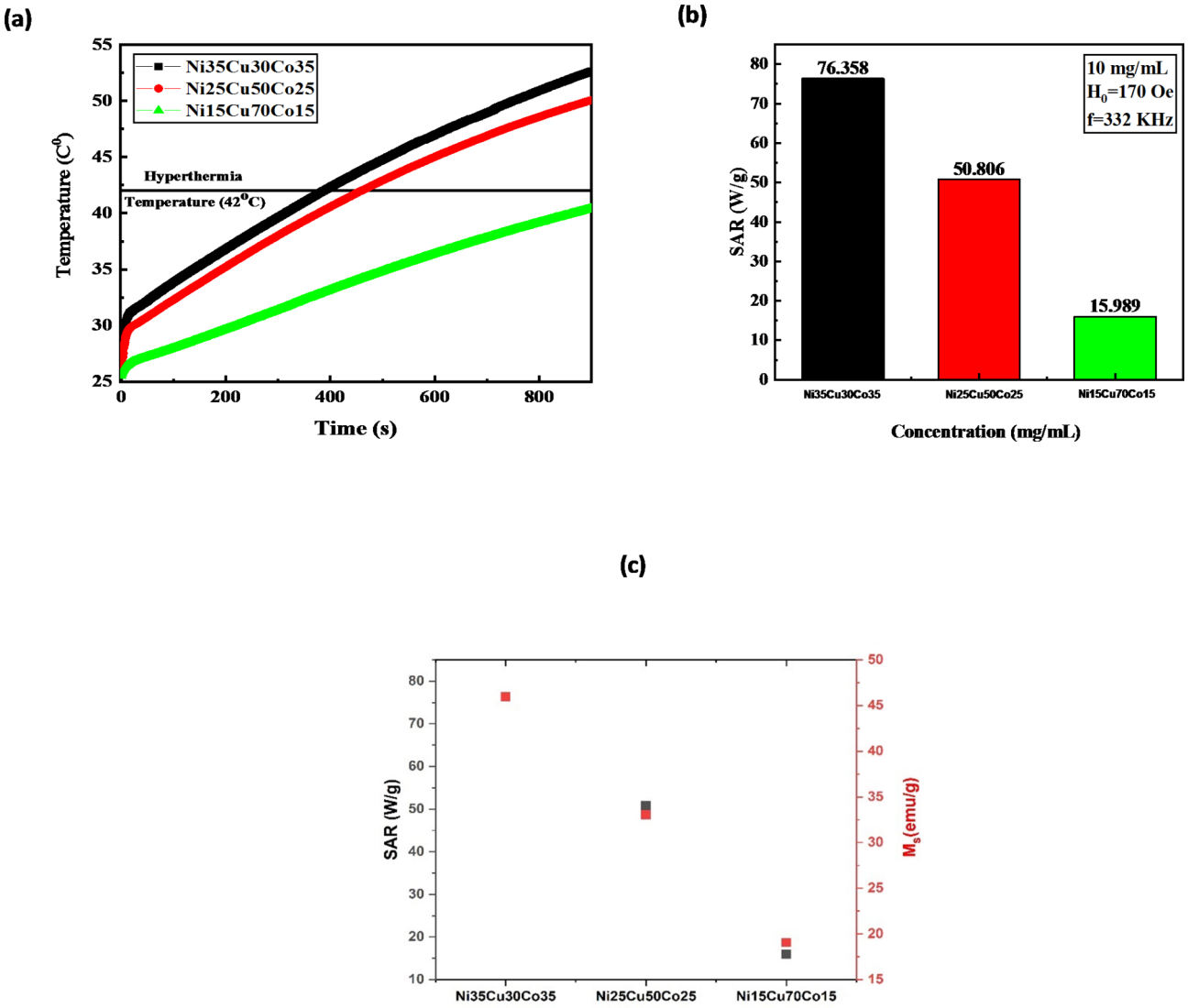

Fig. 12. (**a**) Temperature rise for $Ni_{35}Cu_{30}Co_{35}$, $Ni_{25}Cu_{50}Co_{25}$, and $Ni_{15}Cu_{70}Co_{15}$ (10 mg/mL) at $f = 332$ kHz and $H_0 = 170$ Oe; (**b**,**c**) corresponding SAR values.

Samples	Maximum temperature (°C)	Time needed to reach hyperthermia temperature 42 °C (min)	Ms (emu/g)	SAR (W/g)
$Ni_{35}Cu_{30}Co_{35}$	52.65	6.47	42.63	76.358
$Ni_{25}Cu_{50}Co_{25}$	50.07	7.67	21.49	51.02
$Ni_{15}Cu_{70}Co_{15}$	40.42	Not reaching	4.73	16

Table 5. Heating characteristics of the various nanoalloys (f = 332 kHz and $H_0 = 170$ oe).

NPs is mainly due to the enhancement of interparticle dipolar interactions. The interparticle dipolar interaction, influence the heating ability of MNPs by reducing Neel-Brownian relaxation times. Overall, the heating abilities of the ternary alloys can be tuned for possible use in magnetic hyperthermia by changing many parameters such as concentration, field amplitude, and frequency.

In vitro cell viability

Finally, we explored the anticancer hyperthermal efficacy on cellular activity in the presence and absence of AMF. It is crucial to assess the in vitro toxicity of the as synthesized nanoalloys before employing them for cancer hyperthermia applications. Consequently, the cytotoxicity of $Ni_{25}Cu_{50}Co_{25}$ nanoalloy was evaluated using thiazolyl blue tetrazolium bromide (MTT) cell viability assay against different kinds of metastatic and highly tumorigenic breast cancer cells MDA-MB-231 and KAIMRC2[55]. First, the breast cancer cells were incubated with different concentrations of the nanoalloys for 48 h after which the compound was washed off. Following

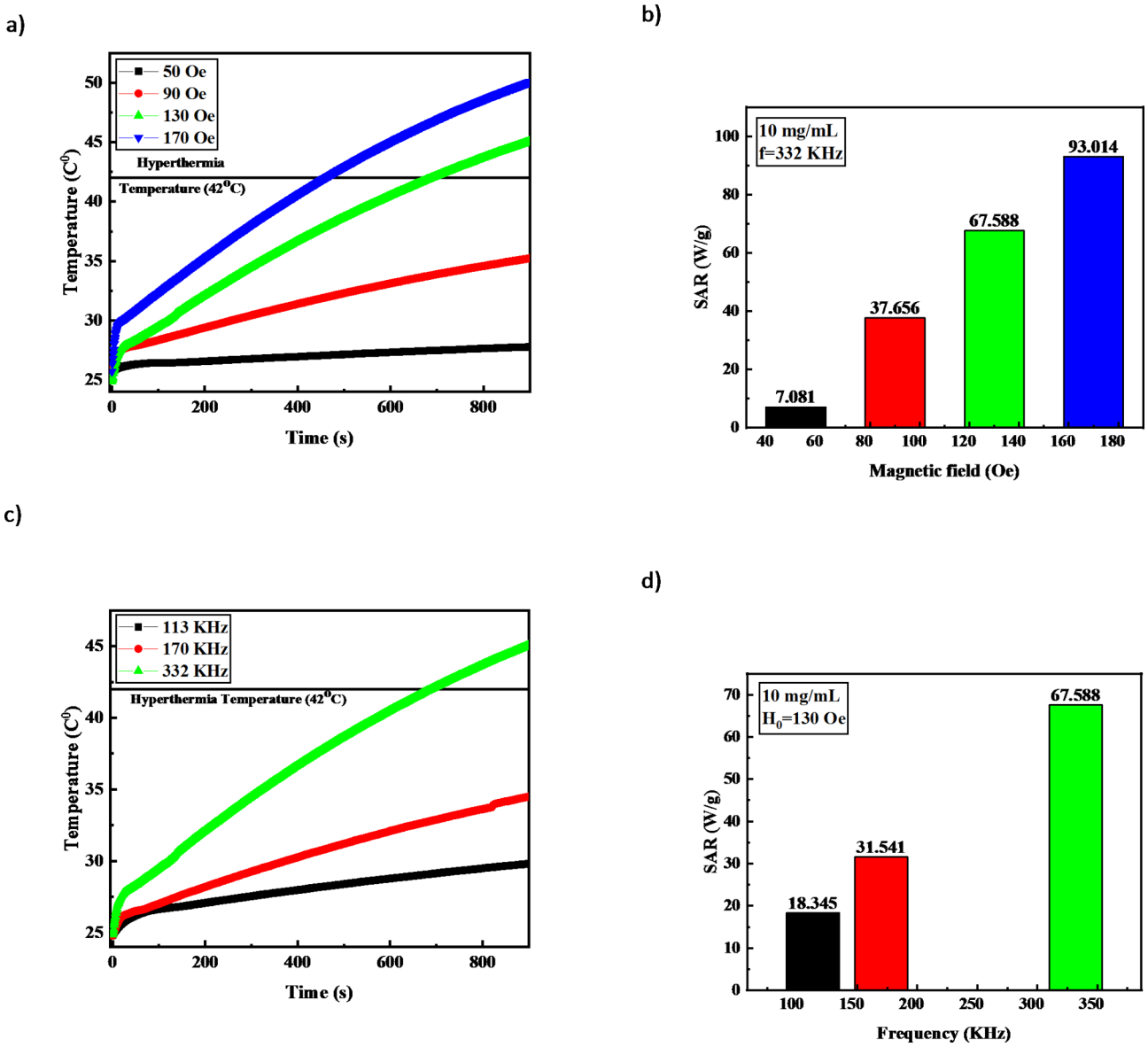

Fig. 13. (**a**,**b**) Temperature rise of $Ni_{25}Cu_{50}Co_{25}$ (10 mg/mL) at different field amplitudes and frequencies; (**c**,**d**) SAR values calculated from the corresponding fields and frequencies.

the addition of the MTT reagent, viability of the cells was then assessed (Fig. 15a). No significant toxicity of the nanoalloys were evident even at the highest NP concentration evaluated. The nanoalloys were found to be slightly more potent to KAIMRC2 as compared to MDA-MB-231 breast cancer cells with proliferation inhibitions (IC_{50}) equal to 1.22 mg/mL and 0.457 mg/mL for MDA-MB-231 and KAIMRC2, respectively (Fig. 15b). As can be seen, KAIMRC2 showed ~2-fold enhanced cytotoxicities in comparison to MDA-MB-231, suggesting improved chances of hyperthermia responses in such cell lines. Importantly, when the same cells were incubated with the free chemotherapeutic drug Mitoxantrone at equivalent concentrations, both MDA-MB-231 and KAIMRC2 cells were completely eradicated (IC_{50} = 0.0019 mg/mL and 0.0014 mg/mL, respectively). This clearly depicts the high cytotoxicity of the free drug towards these metastatic breast cells, suggesting huge potential for the utilization of nanoalloys as promising hyperthermia vehicles. Accordingly, we next investigated the hyperthermal efficiency on KAIMRC2 cell line in the presence and absence of AMF. During the experiment, KAIMRC2 cells alone treated with the nanoalloys (no HT) or treated with the nanoalloys under AMF (HT) were incessantly heated for 15 min under AMF, and MTT viability assay was then evaluated (Fig. 15c). Interestingly, it was found that up to 2-fold enhancement in potency was observed when KAIMRC2 cells were incubated with the nanoalloys in the presence of AMF. These results strongly suggest the effectiveness and the potential promise for using the NiCuCo nanoalloy for magneto-responsive hyperthermia applications.

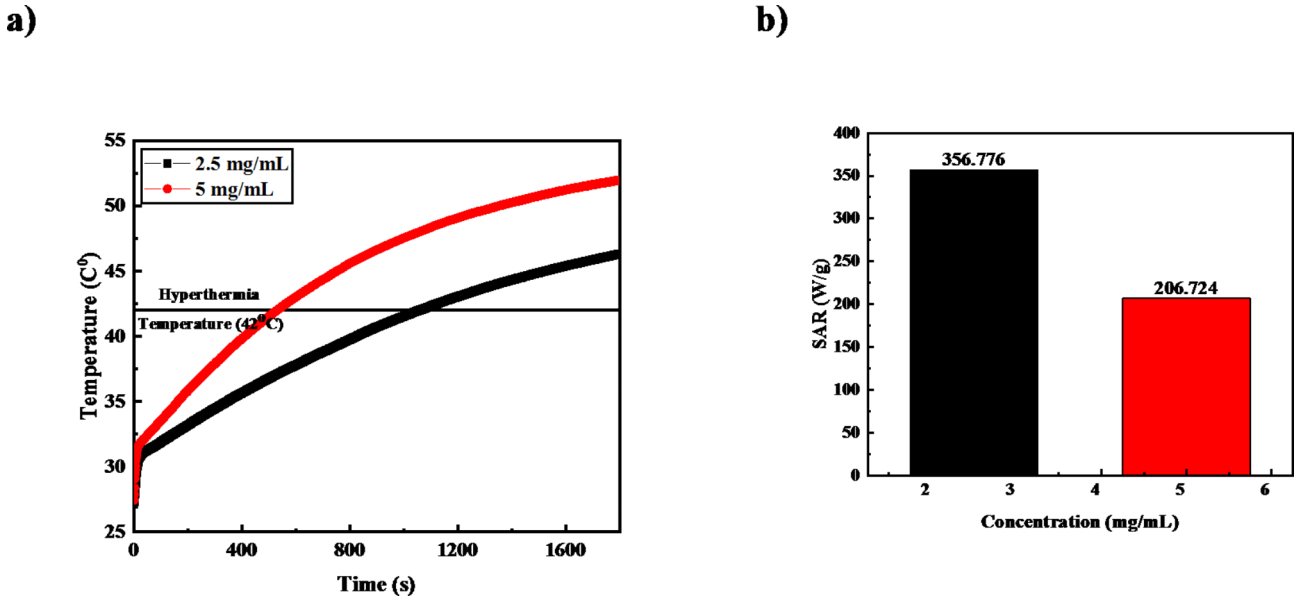

Fig. 14. (**a**) Temperature rise of $Ni_{25}Cu_{50}Co_{25}$ at different concentrations of 2.5 and 5 mg/mL at $f = 332$ kHz and $H_0 = 170$ Oe; (**b**) corresponding SAR values.

Conclusion

In conclusion, we fabricated a set of NiCuCo ternary alloy nanostructures by ball milling, which is a simple and cost-effective method. We indicated that the structure and magnetic properties can be tuned for an efficient heating ability by changing the composition of the alloys. XRD, Rietveld analysis, TEM, SEM-EDX, and DFT calculations were thoroughly investigated elucidating the phase, morphology, size, and crystalline structures of the nanoalloys. Hysteresis loop measurements revealed superparamagnetic behavior and increasing magnetic saturation (M_s) of the NiCuCo alloys with decreasing the Cu percentage ($Ni_{35}Cu_{30}Co_{35} > Ni_{25}Cu_{50}Co_{25} > Ni_{15}Cu_{70}Co_{15}$). DFT calculation corroborated the experimental finding on the structure and magnetic characteristics. We then assessed the heating potentials of the as-prepared NiCuCo nanoalloys, where the highest heating efficiencies and SAR values were attained for $Ni_{35}Cu_{30}Co_{35}$ containing the lowest Cu percentage, directly correlating with the high magnetization saturation obtained. We also showed that the heating abilities can be simply tuned by changing many parameters such as concentration, field amplitude, and frequency. Finally, cytotoxicity viability assays against breast cancer cell lines in the presence and absence of AMF were investigated. No significant decrease in cancer cell viability was observed in the absence of AMF. When tested against tumorigenic KAIMRC2 breast cancer cells under AMF, the NiCuCo nanoalloy was found to be highly potent to the cells (~2-fold enhancement), killing almost all the cells in short times (15 min) and clinically relevant AC magnetic fields ($H_0 = 170$ Oe and $f = 332.8$ kHz). These findings strongly suggest that the as-prepared NiCuCo ternary nanoalloys hold promise for magnetically triggered cancer hyperthermia.

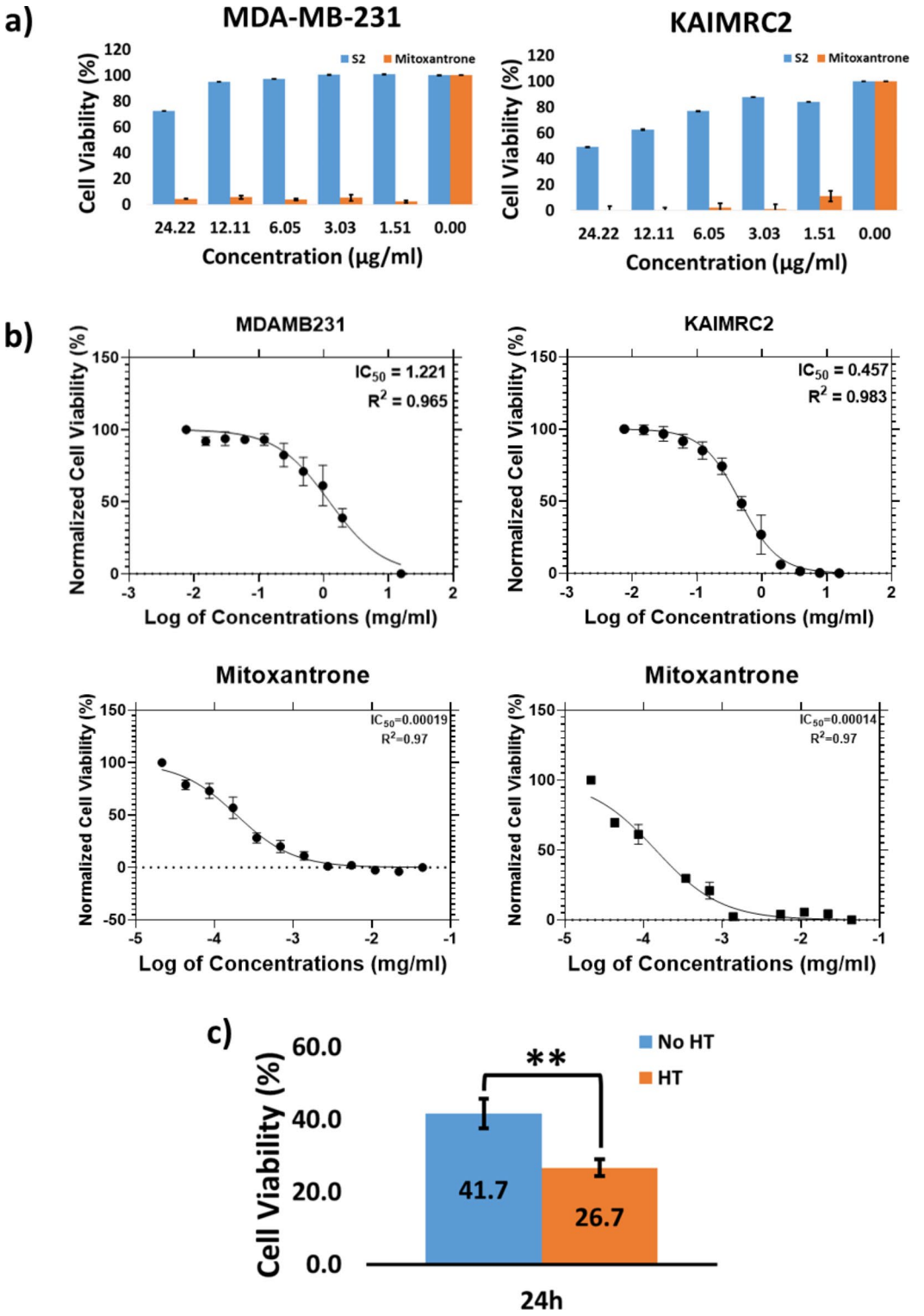

Fig. 15. (**a**) MTT cell viability assays of two different metastatic and tumorigenic breast cancer cell lines (MDA-MB-231 and KIAMRC2) upon incubation with various concentrations of $Ni_{25}Cu_{50}Co_{25}$ nanoalloys or free Mitoxantrone anticancer drug. (**b**) IC_{50} nonlinear regression curves of the corresponding breast cancer cells plotted in dose-dependent concentrations. (**c**) Cellular responses in the presence and absence of AMF: Cell viability percentage for KIAMRC2 treated with or without hyperthermia. The viability of cells was significantly decreased (~ 2-fold) when the cells were exposed to hyperthermia. Experiments were carried out in triplicates and error bars denote standard deviations. (**) indicates $p < 0.005$ and student T-test = 0.003.

Data availability

The datasets generated during and/or analyzed during the current research are available from the corresponding author on reasonable request.

Received: 16 July 2024; Accepted: 15 October 2024
Published online: 23 October 2024

References

1. El-Boubbou, K. Magnetic iron oxide nanoparticles as drug carriers: clinical relevance. *Nanomedicine*. **13** (8), 953–971 (2018).
2. Le Renard, P. E. et al. The in vivo performance of magnetic particle-loaded injectable, in situ gelling, carriers for the delivery of local hyperthermia. *Biomaterials*. **31**, 691–705 (2010).
3. Salunkhe, A. B., Khot, V. M. & Pawar, S. Magnetic hyperthermia with magnetic nanoparticles: a status review. *Curr. Top. Med. Chem.* **14** (5), 572–594 (2014).
4. Jordan, A. et al. Inductive heating of ferrimagnetic particles and magnetic fluids: physical evaluation of their potential for hyperthermia. *Int. J. Hyperth.* **25** (7), 499–511 (2009).
5. Hedayatnasab, Z., Abnisa, F. & Daud, W. M. A. W. Review on magnetic nanoparticles for magnetic nanofluid hyperthermia application. *Mater. Des.* **123**, 174–1961 (2017).
6. Kita, E. et al. Heating characteristics of ferromagnetic iron oxide nanoparticles for magnetic hyperthermia. *J. Appl. Phys.* **107** (9), 09B321 (2010).
7. De la Presa, P. et al. Study of heating efficiency as a function of concentration, size, and applied field in γ-Fe2O3 nanoparticles. *J. Phys. Chem. C*. **116** (48), 25602–25610 (2012).
8. Lemine, O. et al. γ-Fe2O3 by sol–gel with large nanoparticles size for magnetic hyperthermia application. *J. Alloys Compd.* **607**, 125–131 (2014).
9. Thorat, N. D. et al. Superparamagnetic iron oxide nanocargoes for combined cancer thermotherapy and MRI applications. *Phys. Chem. Chem. Phys.* **18** (31), 21331–21339 (2016).
10. Martinez-Boubeta, C. et al. Learning from nature to improve the heat generation of iron-oxide nanoparticles for magnetic hyperthermia applications. *Sci. Rep.* **3** (1), 1–8 (2013).
11. Tadic, M., Kralj, S. & Kopanja, L. Synthesis, particle shape characterization, magnetic properties and surface modification of superparamagnetic iron oxide nanochains. *Mater. Charact.* **148**, 123–133 (2019).
12. Tadić, M. et al. Highly crystalline superparamagnetic iron oxide nanoparticles (SPION) in a silica matrix. *J. Alloys Compd.* **525**, 28–33 (2012).
13. El-Boubbou, K. et al. Evaluating magnetic and thermal effects of various Polymerylated magnetic iron oxide nanoparticles for combined chemo-hyperthermia. *New J. Chem.* **46**, 5489–5504 (2022).
14. Alotaibi, I. et al. Synthesis, characterization and heating efficiency of Gd-doped maghemite (γ-Fe2O3) nanoparticles for hyperthermia application. *Phys. B: Condens. Matter*. **625**, 413510 (2022).
15. Aldaoud, A. et al. Magneto-thermal properties of co-doped maghemite (γ-Fe2O3) nanoparticles for magnetic hyperthermia applications. *Phys. B: Condens. Matter*. **639**, 413993 (2022).
16. Madkhali, N. et al. Heating ability of γ-Fe2O3@ ZnO/Al Nanocomposite for magnetic hyperthermia applications. *Sci. Adv. Mater.* **14** (8), 1394–1400 (2022).
17. Lemine, O. M. et al. El-boubbou, Maghemite (γ-Fe2O3) and γ-Fe2O3-TiO2 nanoparticles for magnetic hyperthermia: synthesis characterization and heating efficiency. *Materials*. **14**, 5691 (2021).
18. Jang, J. et al. Giant magnetic heat induction of magnesium-doped γ-Fe2O3 superparamagnetic nanoparticles for completely killing tumors. *Adv. Mater.* **30** (6), 1704362 (2018).
19. Lemine, O. M., Faqih, A. & Mir, E. L. Effect of Magnesium Ion Substitution on Physical properties and magnetic induction heating of Maghemite (γ-Fe2O3) nanoparticles. *J. Supercond. Novel Magn.* **36** (6), 1583–1593 (2023).
20. Salati, A., Ramazani, A. & Kashi, M. A. Deciphering magnetic hyperthermia propertiesof compositionally and morphologically modulated FeNi nanoparticles using firstorderreversal curve analysis. *Nanotechnology*. **30**, 025707 (2018).
21. Lacroix, L. M. et al. Magnetic hyperthermia in single-domain monodisperse FeCo nanoparticles:evidences for Stoner-Wohlfarth behavior and large losses. *J. Appl. Phys.* **105**, 023911 (2009).
22. Maenosono, S. & Saita, S. Theoretical assessment of FePt nanoparticles as heatingelements for magnetic hyperthermia. *IEEE Trans. Magn.* (2006).
23. Stergar, J. et al. Compounds, the synthesis and characterization of copper–nickel alloy nanoparticles with a therapeutic Curie point using the microemulsion method. *J. Alloys Compd.* **576**, 220–226 (2013).
24. Ban, A. et al. Synthesis of copper–nickel nanoparticles prepared by mechanical milling for use in magnetic hyperthermia. *J. Magn. Magn. Mater.* **323** (17), 2254–2258 (2011).
25. Jiang, Z. et al. Synthesis of core-shell nanowires of FeCoNi alloy core with silicon oxide layers. *Inorg. Chem. Commun.* **7**, 812–814 (2004).
26. Kim, J., Jung, B. M., Lee, S. B. & Kim, K. H. Hyperthermic effects of FeCoNi-coated glassfibers in alternating magnetic field. *IEEE Trans. Magn.* **53**, 7997797 (2017).
27. Salati, A., Ramazani, A. & Kashi, M. A. Tuning hyperthermia properties of FeNiCo ternary alloy nanoparticles by morphological and magnetic characteristics. *J. Magn. Magn. Mater.* **498**, 166172 (2020).
28. Stückler, M. et al. Oxide-stabilized microstructure of severe plastically deformed CuCo alloys. *J. Alloys Compd.* **901**, 163616. https://doi.org/10.1016/j.jallcom.2022.163616 (2022).
29. Ghouri, Z. K., Barakat, N. A. M. & Kim, H. Y. Nfluence of copper content on the electrocatalytic activity toward methanol oxidation of CoχCuy alloy nanoparticles-decorated CNFs. *Sci. Rep.* **5** (1), 16695. https://doi.org/10.1038/srep16695 (2015).
30. Elansary, M. et al. Ovel biocompatible nanomaterial for biomedical application: structural, morphological, magnetic, and in vivo toxicity investigations. *Ceram. Int. S0272884222035404*. https://doi.org/10.1016/j.ceramint.2022.09.341 (2022).
31. Hssaini, A., Belaiche, M. & Elansary, M. One-step synthesis of coated (Gd3+, Er3+) co-doped Co–Ni ferrite nanoparticles; structural and magnetic properties. *J. Mater. Sci. Mater. Electron.* https://doi.org/10.1007/s10854-021-05823-8 (2021).
32. Pei, A. et al. Platinum Island-on-copper–nickel alloy nanoparticle/carbon trimetallic nanocatalyst for selective hydrogenation of cinnamaldehyde. *Catal. Lett.* **151**, 559–572. https://doi.org/10.1007/s10562-020-03295-9 (2021).
33. Mouhib, Y. et al. The first structural, morphological and magnetic property studies on spinel nickel cobaltite nanoparticles synthesized from non-standard reagents. *New. J. Chem.* **47**, 4888–4896. https://doi.org/10.1039/D3NJ00527E (2023).
34. Drouet, C., Laberty, C., Fierro, J. L. G., Alphonse, P. & Rousset, A. X-ray photoelectron spectroscopic study of non-stoichiometric nickel and nickel–copper spinel manganites. *Int. J. Inorg. Mater.* **2**, 419–426 (2000).
35. Xu, L., Yang, Y., Hu, Z. W. & Yu, S. H. Comparison study on the Stability of Copper Nanowires and their oxidation kinetics in gas and liquid. *ACS Nano*. **10**, 3823–3834. https://doi.org/10.1021/acsnano.6b00704 (2016).
36. Ehsan, M. A., Hakeem, A. S. & Rehman, A. Hierarchical growth of CoO nanoflower thin films influencing the electrocatalytic oxygen evolution reaction. *Electrocatalysis*. **11**, 282–291. https://doi.org/10.1007/s12678-020-00585-z (2020).

37. Chai, Z. & Jiang, C. Corrosion behavior and product film formation of NiCoCu nanocrystalline coatings in neutral salt environments. *Electrochim. Acta*. **298**, 616–629 (2019).
38. Hagenmuller, P. D., Deb, K. K., Debbagh, F., de la Rochre, M., Delunas, A. *Mat. Res.* **20**, 1533–1537 (1985).
39. Lee, S., Kang, J. S., Leung, K. T., Kim, S. K. & Sohn, Y. Magnetic Ni-Co alloys induced by water gas shift reaction, Ni-Co oxides by CO oxidation and their supercapacitor applications. *Appl. Surf. Sci.* **386**, 393–404. https://doi.org/10.1016/j.apsusc.2016.06.050 (2016).
40. Arief, I., Mukhopadhyay, P. K., Salunke, O. D. & Tyagi, A. K. Synthesis of dimorphic MR fluid containing NiCo nanoflowers by the polymer assisted polyol method and study of its magnetorheological properties. *Phys. B Condens. Matter* **448**, 73–76. https://doi.org/10.1016/j.physb.2014.04.068 (2014).
41. Jayakumar, H.G. Synthesis and characterization of stoichiometric NiCo nano particles dispersible in both aqueous and non aqueous media. *Solid State Commun.* **149**(41–42), 1769–1771. https://doi.org/10.1016/j.ssc.2009.07.047 (2009).
42. Bai, S. et al. In situ Growth of $Ni_x Co_{100-x}$ Nanoparticles on reduced graphene oxide nanosheets and their magnetic and catalytic properties. *ACS Appl. Mater. Interfaces*. **4**(5), 2378–2386. https://doi.org/10.1021/am300310d (2012).
43. Oulhakem, O., Guetni, I., Elansary, M., Mouhib, Y. & Belaiche, M. Belrhiti Alaoui, characterization and magnetic study of new oleic acid-coated Gd–Sm–Er-doped Co-nanoferrite CoFe1,6Er0,1Gd0,2Sm0,1O4. *Appl. Phys. A*. **127**(11), 814. https://doi.org/10.1007/s00339-021-04941-8 (2021).
44. Mouhib, Y., Belaiche, M., Elansary, M., Ferdi, C. A. & Guetni, I. Multifunctional ferrite nanoparticles prepared from non-standard precursors: structural, morphological, and magnetic study. *J. Mol. Struct.* **1292**, 136094. https://doi.org/10.1016/j.molstruc.2023.136094 (2023).
45. Blaha, P. et al. WIEN2k, An Augmented Plane Wave + Local Orbitals Program for Calculating Crystal Properties (Karlheinz Schwarz, Techn. Universität Wien, Austria), ISBN 3-9501031-1-2. (2018).
46. Perdew, J. P., Burke, K. & Ernzerhof, M. Generalized gradient approximation made simple. *Phys. Rev. Lett.* **77**, 3865. https://doi.org/10.1103/PhysRevLett.77.3865 (1996).
47. Wu, Z. & Cohen, R. E. More accurate generalized gradient approximation for solids. *Phys. Rev. B* **73**(23), 235116. https://doi.org/10.1103/PhysRevB.73.235116 (2006).
48. Grace - https://plasma-gate.weizmann.ac.il/Grace/.
49. Momma, K. & Izumi, F. VESTA 3 for three-dimensional visualization of crystal, volumetric and morphology data. *J. Appl. Crystallogr.* **44** (6), 1272–1276. https://doi.org/10.1107/S0021889811038970 (2011).
50. Moussa, R., Abdiche, A., Khenata, R. & Soyalp, F. First principles calculation of the structural, electronic, optical and elastic properties of the cubic AlxGa1-xSb ternary alloy. *Opt. Mater.* **113**, 110850. https://doi.org/10.1016/j.optmat.2021.110850 (2021).
51. El Haj, F., Akbarzadeh, H. & Hassan & First-principles investigation of BNxP1 – x, BNxAs1 – x and BPxAs1 – x ternary alloys. *Mater. Sci. Eng. B.* **121**(1), 170–177. https://doi.org/10.1016/j.mseb.2005.03.019 (2005).
52. Moon, R. M. Distribution of magnetic moment in hexagonal cobalt. *Phys. Rev.* **136**(1A), A195–A202. https://doi.org/10.1103/PhysRev.136.A195 (1964).
53. Zamudio-Bayer, V. et al. Large orbital magnetic moments of small, free cobalt cluster ions Con^+ with $n \leq 9$. *J. Phys. Condens. Matter* **30**(46), 464002. https://doi.org/10.1088/1361-648X/aae54a (2018).
54. W. Feng, Y. Qi, S. Wang, Effects of Mn and Al addition on structural and magnetic properties of FeCoNi-based high entropy alloys, Mater. Res. Express, vol. 5, no. 10, p. 106511, (2018). doi: 10.1088/2053-1591/aadaa7.
55. Ali, R. et al. Isolation and establishment of a highly proliferative, Cancer Stem Cell-Like, and naturally immortalized triple-negative breast Cancer cell line, KAIMRC2. *Cells*. **10**, 1303. https://doi.org/10.3390/cells10061303 (2021).

Acknowledgements

The authors thank Imam Mohammad Ibn Saud Islamic University's Deanship of Scientific Research for financing and supporting this work through the Graduate Student Research Support Program.

Author contributions

"O.M L wrote the original draft, analysis, investigation, N.A: Formal analysis; Investigation, M.E: XRD analysis C.A.F: DFT M. S.A: SQUID S.A : Prepared figures heating, analysis, N.M: Analysis, Heating ability, R.A: Toxicity and in-vitro A.Z.A: SEM/EDAX, M.B: review & editing) K.E: reviewed & editing), All authors reviewed the manuscript".

Declarations

Competing interests

The authors declare no competing interests.

Additional information

Correspondence and requests for materials should be addressed to O.M.L.

Reprints and permissions information is available at www.nature.com/reprints.

Publisher's note Springer Nature remains neutral with regard to jurisdictional claims in published maps and institutional affiliations.